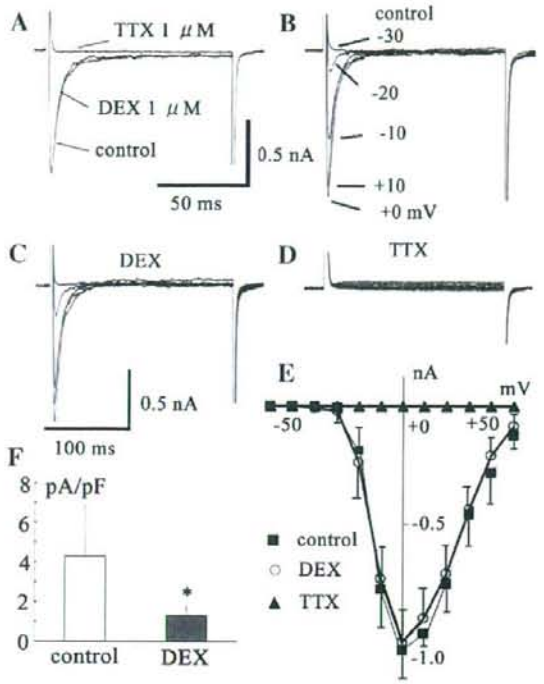

Fig. 1. Voltage-gated Na^+ channels (I_{Na}) and the effects of dexamethasone (DEX) in cultured human bronchial smooth muscle cells (hBSMCs). (A) Acute effects of DEX on I_{Na}. The cell was held at −80 mV, and depolarizing pulses at +0 mV were applied at 0.2 Hz. The current traces are shown in control, ~5 min after the application of DEX (1 μM), and in the presence of TTX (1 μM). The data are representative of 5 different experiments. (B–E) Effects of DEX on I_{Na}. The cell was held at −80 mV, and the command voltage pulses to various membrane potentials are applied. The original current traces elicited by various depolarizing pulses are indicated in control (B) and in the presence of DEX (1 μM, C) for 5 min, and in the presence of TTX (1 μM, D). The current–voltage (*I–V*) relations (control, closed squares; DEX, open circle; TTX, closed triangle) measured at the peak after the leakage currents were subtracted are illustrated in E. The data represent the mean value± S.E.M. from four different cells. (F) Effect of chronic treatment of dexamethasone on I_{Na}. The cells were treated with dexamethasone (1 μM) or without (control) for 48 h. The current-density of I_{Na} adjusted by cell capacitance in cells with I_{Na} was shown in control cells and cells treated with dexamethasone. *P<0.01 vs. control.

molecular size, identical to cDNA fragments amplified from reversely transcripted mRNA. In addition, expression of SCN channel family members (SCN1A, 2A, 3A, 4A, 5A, 6A, 8A and 9A) was also investigated by quantitative real-time RT-PCR. Expression of SCN10A and 11A was not investigated in this study, because these genes form TTX-insensitive I_{Na}. Transcript levels were normalized to 18S ribosomal housekeeping gene. As shown in Fig. 2B, expression levels of SCN9A mRNA were much higher than those of the other SCN families (SCN2A, 3A, 8A). The expression of SCN1A, 4A, 5A, 6A was not detected. Thus, it is likely that I_{Na} expressed in these cells is mainly composed of $Na_V1.7$ encoded by SCN9A as previously described (Jo et al., 2004).

Fig. 2C and D shows the effects of dexamethasone on SCN9A mRNA steady-state levels. To study this, we treated cells in the culture medium with or without dexamethasone (1 μM) for 24–48 h, and measured steady-state levels of SCN9A mRNA. Fig. 2C shows the effects of chronic treatment with dexamethasone on the expression of SCN9A mRNA by using conventional RT-PCR. The cells were treated with and without dexamethasone (1 μM). Treatment with dexamethasone for 24 h inhibited the expression of SCN9A mRNA, compared with the internal control (GAPDH). To confirm it, the expression of SCN9A mRNA was investigated by real-time quantitative RT-PCR, and transcript levels were normalized to 18S ribosomal housekeeping gene. As shown in Fig. 2D, treatment with dexamethasone (1 μM) for 24–48 h significantly decreased SCN9A mRNA expression, compared with that in control samples.

I_{Na} is composed of a pore-forming α subunit encoded by SCN family and auxiliary β subunit, and four kinds of β subunit mRNA (SCNβ1–4) have been identified until now. Expression of SCNβ channel family members (SCNβ1–4) was investigated by quantitative real-time RT-PCR in cultured human bronchial smooth muscle cells, and compared with normal human left ventricle (Fig. 3). In human adult heart (Fig. 3A), β subunits were mainly composed of SCNβ1 and SCNβ2, while they are mainly composed of SCNβ1 in cultured human bronchial smooth muscle cells (Fig. 3B). Fig. 3B also shows the effects of dexamethasone on SCNβ mRNA. Cultured human bronchial smooth muscle cells were treated with or without dexamethasone (1 μM) for 24 h, and the steady-state levels of SCNβ mRNA were measured. In contrast to the effects of dexamethasone on SCN9A mRNA, dexamethasone (1 μM) did not change the SCNβ mRNA levels significantly. Thus, dexamethasone appears to selectively affect the expression of SCN α subunit mRNA, but not auxiliary β subunit mRNA.

The effects of various concentrations of dexamethasone (10^{-10}–10^{-6} M) were also investigated in Fig. 4A. Dexamethasone decreased the mRNA steady-state levels in a concentration-dependent manner. Significant inhibitory effects were observed at concentrations higher than 0.1 nM. Fig. 4B shows the effects of spironolactone, a mineral corticoid receptor blocker, and mifepristone, a glucocorticoid receptor blocker on the action of dexamethasone. The inhibitory effect of dexamethasone (100 nM) on SCN9A mRNA was not blocked by spironolactone (1 μM), but significantly inhibited by mifepristone (1 μM). Similarly, mifepristone (10 μM), but not spironolactone (10 μM), antagonized the effects of dexamethasone (1 μM) on SCN9A mRNA. These results suggest that dexamethasone inhibits SCN9A mRNA expression via the glucocorticoid receptor.

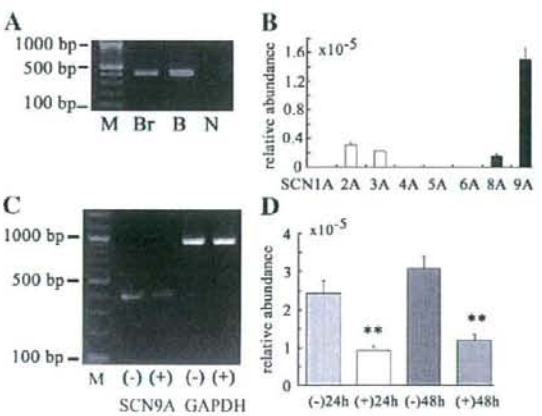

Fig. 2. Effects of chronic treatment of dexamethasone (Dex) on the mRNA steady-state levels of SCN9A in cultured human bronchial smooth muscle cells (hBSMCs). (A) Expression of SCN9A mRNA detected by RT-PCR. PCR cycle is 35. M: Marker, Br (human fetal brain); B (hBSMCs), N (negative) (B) The quantitative real-time RT-PCR. The expression levels of SCN channel family genes (SCN1A, 2A, 3A, 4A, 5A, 6A, 8A and 9A) were normalized to those of the 18S ribosomal RNA levels. Data are means±S.E.M. from six independent samples. (C) RT-PCR analysis of SCN9A and GAPDH. Cells were treated with and without Dex (1 μM) for 24 h in culture medium. PCR cycle is 28. (D) Effects of Dex on SCN9A mRNA expression by using quantitative real-time RT-PCR. The expression of SCN9A mRNA was evaluated by quantitative real-time RT-PCR, and transcript levels were normalized to 18S ribosomal housekeeping gene. The level of mRNA expression of SCN9A in the presence of Dex for various intervals (24–48 h) was compared with that in the absence of Dex (control). The data represent the mean value ±S.E.M. from four different cells. **P<0.01 vs. control.

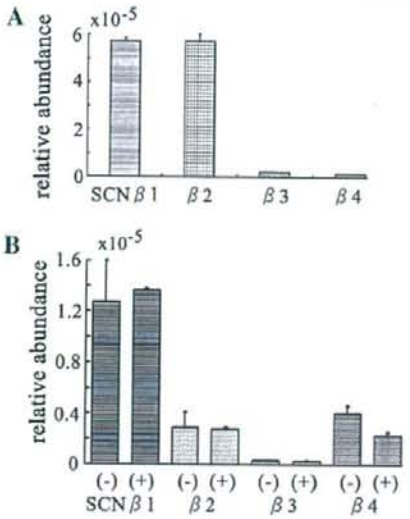

Fig. 3. (A) Expression of SCNβ1–4 in human adult heart. (B) Effects of dexamethasone (Dex) on the mRNA steady-state levels of SCNβ subunit in cultured human bronchial smooth muscle cells. In B, cells were treated with and without Dex (1 μM) for 24 h. The expression of SCNβ1–4 mRNA was evaluated by quantitative real-time RT-PCR, and transcript levels were normalized to 18S ribosomal housekeeping gene. The level of mRNA expression of SCNβ1–4 in the presence of Dex was compared with that in the absence of Dex. Each data represent the mean value ± S.E.M. from four different cells.

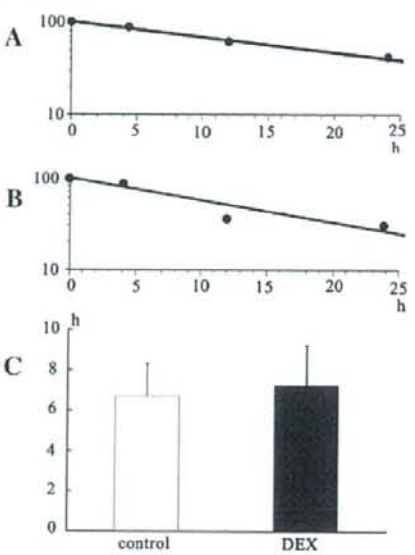

Fig. 5. Effects of dexamethasone on SCN9A mRNA half-life. Cells were exposed to dexamethasone (1 μM) for 24 h and to actinomycin D for various time intervals. All time points were normalized to time 0 for that given condition (with (A) or without dexamethasone (B)); therefore, all time 0 points start as 100%. Typical data are shown in A and B. The data were shown as the normalized mRNA levels for the different time points measured by quantitative RT-PCR analysis. The data were best fit by a linear line. (C) SCN9A mRNA half-life in control and dexamethasone-treated cells. The data represent the mean value ± S.E.M. from four different experiments included in A and B.

Effects of dexamethasone on SCN9A mRNA half-life

We investigated whether the decreased mRNA steady-state levels induced by dexamethasone were related to changes in half-life of SCN9A mRNA. Cells were treated with actinomycin D for various intervals to inhibit transcription and mRNA levels for the different time points were measured and plotted on a log scale, and the half-life was calculated. Each time point was normalized to time 0 for that specific condition (with and without dexamethasone). Fig. 5A and B shows typical data of the calculated half-life. It was 7.9 h for dexamethasone-treated cells (Fig. 5A) and 5.3 h for control cells (Fig. 5B). Similarly, the calculated half-life was not statistically different in between control (6.7 ± 1.6 h, $n=4$) and dexamethasone-treated cells (7.2 ± 2.0 h, $n=4$) as shown in Fig. 5C. Therefore, the decreased SCN9A mRNA levels by dexamethasone were not due to a decrease in mRNA half-life.

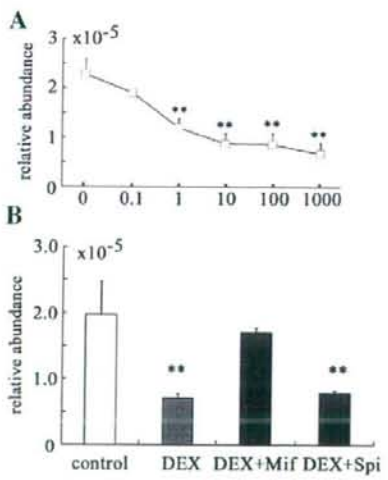

Fig. 4. (A) Concentration-dependent effects of dexamethasone (Dex) on the mRNA steady-state levels of SCN9A. Cells were exposed to the indicated concentrations (0.1–1000 nM) of Dex for 24 h. (B) Effects of spironolactone (Spi, 1 μM) and mifepristone (Mif, 1 μM) on the inhibitory actions of Dex. Cells were treated with Dex (100 nM) for 24 h in the presence or absence of these agents. In A and B, the expression of SCN9A mRNA was evaluated by real-time quantitative RT-PCR, and transcript levels were normalized to 18S ribosomal RNA. The data represent the mean value ± S.E.M. from four different cells. *$P<0.01$ vs. control.

Discussion

The present study provides the first evidence that dexamethasone failed to affect I_{Na} directly, but dexamethasone inhibited I_{Na} encoded by SCN9A mRNA in cultured human bronchial smooth muscle cells by inhibiting the transcription via the glucocorticoid receptor.

Airway smooth muscle plays a principal role in the pathogenesis of airway remodeling and then asthma (Hirst and Lee, 1998; Hirst et al., 2000; Johnson et al., 2001; Vignola et al., 2001), where increased airway smooth muscle content and subsequently airway wall thickening are occurring as a result of proliferative and/or hypertrophic growth of smooth muscle cells. Primary cultures are being used to investigate airway myocyte proliferation and hypertrophy (Hall and Kotlikoff, 1995). In vitro, when airway smooth muscle is stimulated to proliferate, the muscle differentiates from a contractile phenotype to a more synthetic one (Chamley-Campbell et al., 1979). Similarly, chronic stimulation by cytokines or growth factors in the inflamed airway walls of asthmatic subjects results in the proliferation and dedifferentiation of the airway smooth muscle, making it more synthetic (Halayko et al., 1999). I_{Na} is not expressed in freshly isolated tonic smooth muscle cells such as bronchial smooth muscle, while it

has been identified under the cultured conditions (Snetkov et al., 1996; Quignard et al., 1997; Cox et al., 1998; Boccara et al., 1999; Choby et al., 2000a; Choby et al., 2000b; Jo et al., 2004). The present study also showed the presence of I_{Na} in cultured human bronchial smooth muscle cells. Thus, the expression of I_{Na} may be related to the culture conditions, where cell proliferation or differentiation may be involved as previously described ((Snetkov et al., 1996; Quignard et al., 1997; Cox et al., 1998; Boccara et al., 1999; Choby et al., 2000a; Choby et al., 2000b). These changes also occur under various pathophysiological conditions such as asthma (Hirst et al., 2000; Johnson et al., 2001; Vignola et al., 2001), proposing that the expression of I_{Na} may play a role in these pathophysiological conditions. However, since it is difficult to get freshly isolated human preparations, the possible expression of I_{Na} under these conditions is worth considering and further studies are necessary to clarify the physiological significance of the channel.

Glucocorticoids are the most effective therapy currently available for the treatment of asthma, and have been reported to affect ionic channels and then the electrical activity of excitable cells by regulating the transcription (Takimoto et al., 1993; Takimoto and Levitan, 1994; Chalaka et al., 1999). Glucocorticoids have been known to affect the expression of Na^+–K^+ ATPase (Chalaka et al., 1999) and several ion channels such as $K_V1.5$, a non-inactivating K^+ current (Takimoto et al., 1993; Takimoto and Levitan, 1994). Dexamethasone has been also reported to downregulate voltage-gated Na^+ channel in clonal rat pituitary cells, by using patch-clamp techniques, and saxitoxin binding assay (Avila et al., 2003). In the present study, short-term application of dexamethasone did not affect I_{Na} significantly. On the other hand, chronic treatment with dexamethasone inhibited SCN9A mRNA levels, and also reduced the current-density of the channel. The analysis of the protein level by using Western blotting was lacking, because the suitable antibody for human $Na_V1.7$ could not be obtained. However, these results suggest that dexamethasone affects the expression of voltage-gated Na^+ channel, by inhibiting the transcription. The significant inhibitory effects were observed at concentrations higher than 0.1 nM. The effect of dexamethasone on SCN9A mRNA was not blocked by spironolactone, a mineral corticoid receptor blocker, but inhibited by mifepristone, a glucocorticoid receptor blocker, suggesting that dexamethasone inhibits SCN9A mRNA expression via the glucocorticoid receptor. The exact mechanism by which dexamethasone inhibits SCN9A mRNA has not been elucidated. But, our study using the RNA stability results indicates that dexamethasone inhibited transcription of SCN9A gene as a mechanism of inhibiting mRNA steady-state levels. Dexamethasone has been reported to inhibit mitogen-stimulated DNA syntheses and proliferation of smooth muscle including human airways by inducing an arrest in the G1 phase of the cell cycle (Stewart et al., 1995; Dixon et al., 1999). However, in our experimental conditions using fetal bovine serum, human epidermal growth factor, insulin, and human fibroblast growth factor as mitogens, dexamethasone did not inhibit cell proliferation significantly (data not shown). Dixon et al. (1999) also showed that the inhibitory effect of dexamethasone on DNA synthesis was variable depending on the growth factors: significant effect was observed on beta-hexosaminidase A and insulin; no significant effect was observed on epidermal growth factor and fetal bovine serum. Thus, it is unlikely that the antiproliferative effects of glucocorticoids may contribute to underlie the mechanism of the inhibitory effects of dexamethasone on I_{Na} in cultured human bronchial smooth muscle cells.

I_{Na} is composed of a pore-forming α subunit encoded by SCN family and auxiliary β subunit (Catterall, 1993; Goldin, 1999; Goldin, 2002). Until now, four kinds of β subunit mRNA (SCNβ1–4) have been identified, and the abnormality of β subunits has been reported. The increase of SCN1β mRNA has been reported in lung tissues from patients with idiopathic and familial pulmonary arterial hypertension (Geraci et al., 2001). In the present study, β subunits were mainly composed of SCNβ1 in cultured human bronchial smooth muscle cells. Thus, it is most likely that I_{Na} expressed in cultured human bronchial smooth muscle cells is encoded by SCN9A and SCNβ1. Dexamethasone did not affect SCNβ1 mRNA in comparison with SCN9A mRNA, suggesting that dexamethasone may affect I_{Na} by selectively inhibiting the transcription of SCN9A.

Physiological significance of I_{Na} expressed in cultured human bronchial smooth muscle cells remains unclear. But, it seems likely that the activation of I_{Na} induces an increase of Na influx and intracellular Na^+ concentration ($[Na^+]_i$). The increase in $[Na^+]_i$ may activate the reverse mode Na^+/Ca^{2+} exchanger, which may subsequently raise intracellular Ca^{2+} concentration (Boccara et al., 1999; Saleh et al., 2005). Thus, I_{Na} may alter cell excitability, contractility, and remodeling of human bronchial smooth muscle cells. The present study showed that chronic treatment of dexamethasone inhibited I_{Na} expression, proposing that dexamethasone may reduce the excitation–contraction coupling, and then smooth muscle tone via regulation of I_{Na} expression. Alternatively, Na^+ influx through I_{Na} may regulate cell volume (Bortner and Cidlowski, 2003), induce changes in ion flux, and affect the cytoskeleton, protein kinase activity and gene expression. These effects of I_{Na} may enhance cellular behaviours linked to secretion and motilities in cultured human bronchial smooth muscle cells as reported in cancer cells (Mycielska et al., 2003; Fraser et al., 2003; Onganer and Djamgoz, 2005). Further studies are needed to clarify the physiological significance of I_{Na} in cultured human bronchial smooth muscle cells.

Conclusion

The present study provides the evidence that dexamethasone failed to affect I_{Na} directly, but dexamethasone inhibited I_{Na} encoded by SCN9A mRNA in cultured human bronchial smooth muscle cells by inhibiting the transcription via the glucocorticoid receptor.

References

Avila, G., Monjaraz, E., Espinosa, J.L., Cota, G., 2003. Downregulation of voltage-gated sodium channels by dexamethasone in clonal rat pituitary cells. Neuroscience letters 339 (1), 21–24.

Barnes, P.J., 1996. Mechanisms of action of glucocorticoids in asthma. American Journal of Respiratory and Critical Care Medicine 154 (2 Pt 2), S21–S26.

Belevych, A.E., Zima, A.V., Vladimirova, I.A., Hirata, H., Jurkiewicz, A., Jurkiewicz, N.H., Shuba, M.F., 1999. TTX-sensitive Na^+ and nifedipine-sensitive Ca^{2+} channels in rat vas deferens smooth muscle cells. Biochimica et Biophysica Acta 1419 (2), 343–352.

Boccara, G., Choby, C., Frapier, J.M., Quignard, J.F., Nargeot, J., Dayanithi, G., Richard, S., 1999. Regulation of Ca^{2+} homeostasis by atypical Na^+ currents in cultured human coronary myocytes. Circulation Research 85 (7), 606–613.

Bortner, C.D., Cidlowski, J.A., 2003. Uncoupling cell shrinkage from apoptosis reveals that Na^+ influx is required for volume loss during programmed cell death. The Journal of Biological Chemistry 278 (40), 39176–39184.

Catterall, W.A., 1993. Structure and function of voltage-gated ion channels. Trends in Neurosciences 16 (12), 500–506.

Chalaka, S., Ingbar, D.H., Sharma, R., Zhau, Z., Wendt, C.H., 1999. Na^+–K^+-ATPase gene regulation by glucocorticoids in a fetal lung epithelial cell line. American Journal of Physiology 277 (1 Pt 1), L197–L203.

Chamley-Campbell, J., Campbell, G.R., Ross, R., 1979. The smooth muscle cell in culture. Physiological Reviews 59 (1), 1–61.

Choby, C., Mangoni, M.E., Boccara, G., Nargeot, J., Richard, S., 2000a. Evidence for tetrodotoxin-sensitive sodium currents in primary cultured myocytes from human, pig and rabbit arteries. Pflugers Archiv European Journal of Physiology 440 (1), 149–152.

Choby, C., Quignard, J.F., Boccara, G., Mangoni, M., Frapier, J.M., Albat, B., Nargeot, J., Richard, S., 2000b. Is atypical sodium current related to arterial pathophysiology? Archives des Maladies du Coeur et des Vaisseaux 93 (8), 1003–1008.

Cox, R.H., Zhou, Z., Tulenko, T.N., 1998. Voltage-gated sodium channels in human aortic smooth muscle cells. Journal of Vascular Research 35 (5), 310–317.

Dixon, E.R., Weinberg, J.A., Lew, D.B., 1999. Effect of dexamethasone on bovine airway smooth muscle cell proliferation. The Journal of Asthma 36 (6), 519–525.

Fraser, S.P., Salvador, V., Manning, E.A., Mizal, J., Altun, S., Raza, M., Berridge, R.J., Djamgoz, M.B., 2003. Contribution of functional voltage-gated Na^+ channel expression to cell behaviors involved in the metastatic cascade in rat prostate cancer: I. Lateral motility. Journal of Cellular Physiology 195 (3), 479–487.

Geraci, M., Moore, M., Gesell, T., Yeager, M., Alger, L., Golpon, H., Gao, B., Loyd, J.E., Tuder, R.M., Voelkel, N.F., 2001. Gene expression patterns in the lungs of patients with primary pulmonary hypertension: a gene microarray analysis. Circulation Research 88 (6), 555–562.

Goldin, A.L., 1999. Diversity of mammalian voltage-gated sodium channels. Annals of the New York Academy of Sciences 868, 38–58.
Goldin, A.L., 2002. Evolution of voltage-gated Na+ channels. The Journal of Experimental Biology 205 (Pt 5), 575–584.
Halayko, A.J., Camoretti-Mercado, B., Forsythe, S.M., Vieira, J.E., Mitchell, R.W., Wylam, M.E., Hershenson, M.B., Solway, J., 1999. Divergent differentiation paths in airway smooth muscle culture: induction of functionally contractile myocytes. American Journal of Physiology 276 (1 Pt 1), L197–L206.
Hall, I.P., Kotlikoff, M., 1995. Use of cultured airway myocytes for study of airway smooth muscle. American Journal of Physiology 268 (1 Pt 1), L1–L11.
Hamill, O.P., Marty, A., Neher, E., Sakmann, B., Sigworth, F.J., 1981. Improved patch-clamp techniques for high-resolution current recording from cells and cell-free membrane patches. Pflugers Archiv European Journal of Physiology 391 (2), 85–100.
Hirst, S.J., Lee, T.H., 1998. Airway smooth muscle as a target of glucocorticoid action in the treatment of asthma. American Journal of Respiratory and Critical Care Medicine 158 (5 Pt 3), S201–S206.
Hirst, S.J., Walker, T.R., Chilvers, E.R., 2000. Phenotype diversity and molecular mechanisms of airway smooth muscle proliferation in asthma. The European Respiratory Journal 16 (1), 159–177.
Hollywood, M.A., Cotton, K.D., Thornbury, K.D., McHale, N.G., 1997. Tetrodotoxin-sensitive sodium current in sheep lymphatic smooth muscle. Journal of Physiology 503 (Pt 1), 13–20.
Jo, T., Nagata, T., Iida, H., Imuta, H., Iwasawa, K., Ma, J., Hara, K., Omata, M., Nagai, R., Takizawa, H., Nagase, T., Nakajima, T., 2004. Voltage-gated sodium channel expressed in cultured human smooth muscle cells: involvement of SCN9A. FEBS letters 567 (2–3), 339–343.
Johnson, P.R., Roth, M., Tamm, M., Hughes, M., Ge, Q., King, G., Burgess, J.K., Black, J.L., 2001. Airway smooth muscle cell proliferation is increased in asthma. American Journal of Respiratory and Critical Care Medicine 164, 474–477.
Kim, J., McKinley, L., Siddiqui, J., Bolgos, G.L., Remick, D.G., 2004. Prevention and reversal of pulmonary inflammation and airway hyperresponsiveness by dexamethasone treatment in a murine model of asthma induced by house dust. American Journal of Physiology 287 (3), L503–L509.
Kumar, R.K., Herbert, C., Thomas, P.S., Wollin, L., Beume, R., Yang, M., Webb, D.C., Foster, P.S., 2003. Inhibition of inflammation and remodeling by roflumilast and dexamethasone in murine chronic asthma. The Journal of Pharmacology and Experimental Therapeutics 307 (1), 349–355.
Mycielska, M.E., Fraser, S.P., Szatkowski, M., Djamgoz, M.B., 2003. Contribution of functional voltage-gated Na+ channel expression to cell behaviors involved in the metastatic cascade in rat prostate cancer: II. Secretory membrane activity. Journal of Cellular Physiology 195 (3), 461–469.
Nakajima, T., Iwasawa, K., Oonuma, H., Imuta, H., Hazama, H., Asano, M., Morita, T., Nakamura, F., Suzuki, J., Suzuki, S., Kawakami, Y., Omata, M., Okuda, Y., 1999. Troglitazone inhibits voltage-dependent calcium currents in guinea pig cardiac myocytes. Circulation 99 (22), 2942–2950.
Onganer, P.U., Djamgoz, M.B., 2005. Small-cell lung cancer (human): potentiation of endocytic membrane activity by voltage-gated Na+ channel expression in vitro. The Journal of Membrane Biology 204 (2), 67–75.
Oonuma, H., Iwasawa, K., Iida, H., Nagata, T., Imuta, H., Morita, Y., Yamamoto, K., Nagai, R., Omata, M., Nakajima, T., 2002. Inward rectifier K+ current in human bronchial smooth muscle cells: inhibition with antisense oligonucleotides targeted to Kir2.1 mRNA. American Journal of Respiratory Cell and Molecular Biology 26 (3), 371–379.
Quignard, J.F., Ryckwaert, F., Albat, B., Nargeot, J., Richard, S., 1997. A novel tetrodotoxin-sensitive Na+ current in cultured human coronary myocytes. Circulation Research 80 (3), 377–382.
Saleh, S., Yeung, Y.M., Prestwich, S., Pucovsky, V., Greenwood, I., 2005. Electrophysiological and molecular identification of voltage-gated sodium channels in murine vascular myocytes. Journal of Physiology 568 (Pt 1), 155–169.
Snetkov, V.A., Hirst, S.J., Ward, J.P., 1996. Ion channels in freshly isolated and cultured human bronchial smooth muscle cells. Experimental Physiology. 81 (5), 791–804.
Stewart, A.G., Fernandes, D., Tomlinson, P.R., 1995. The effect of glucocorticoids on proliferation of human cultured airway smooth muscle. British Journal of Pharmacology 116 (8), 3219–3226.
Takimoto, K., Levitan, E.S., 1994. Glucocorticoid induction of Kv1.5 K+ channel gene expression in ventricle of rat heart. Circulation Research 75 (6), 1006–1013.
Takimoto, K., Fomina, A.F., Gealy, R., Trimmer, J.S., Levitan, E.S., 1993. Dexamethasone rapidly induces Kv1.5 K+ channel gene transcription and expression in clonal pituitary cells. Neuron 11 (2), 359–369.
Terasawa, K., Nakajima, T., Iida, H., Iwasawa, K., Oonuma, H., Jo, T., Morita, T., Nakamura, F., Fujimori, Y., Toyo-oka, T., Nagai, R., 2002. Nonselective cation currents regulate membrane potential of rabbit coronary arterial cell: modulation by lysophosphatidylcholine. Circulation 106 (24), 3111–3119.
Vignola, A.M., Gagliardo, R., Siena, A., Chiappara, G., Bonsignore, M.R., Bousquet, J., Bonsignore, G., 2001. Airway remodeling in the pathogenesis of asthma. Current Allergy and Asthma Reports 1 (2), 108–115.
Xiong, Z., Sperelakis, N., Noffsinger, A., Fenoglio-Preiser, C., 1993. Fast Na+ current in circular smooth muscle cells of the large intestine. Pflugers Archiv European Journal of Physiology 423 (5–6), 485–491.

Sequential and Quantitative Analysis of a Murine Model of Elastase-Induced Emphysema

Masaki KAWAKAMI,[a,b] Yukiko MATSUO,[a] Kenta YOSHIURA,[a] Takahide NAGASE,[b] and Naomi YAMASHITA*,[a]

[a] *Department of Pharmatherapy, Research Institute of Pharmaceutical Sciences, Musashino University; 1–1–20 Shinmachi, Nishitokyo, Tokyo 202–8585, Japan; and* [b] *Department of Pulmonary Medicine, Faculty of Medicine, University of Tokyo; 7–3–1 Hongo, Bunkyo-ku, Tokyo 113–0033, Japan.*

Received January 8, 2008; accepted May 7, 2008; published online May 8, 2008

Emphysema, one of chronic obstructive pulmonary disease (COPD), is characterized as destruction of airway wall and small airway inflammation. To assess the kinetics of disease progression in murine model of elastase-induced emphysema, we used micro-computed tomography (CT) compared with morphological changes. Two week after elastase administration, a significant increase in the volume of low-density areas, recognized as −800—−600 Hounsfield units by micro-CT, was observed. Coefficient of correlation between mean linear intercept (Lm) and low-density area examined by CT, was 0.79 ($p<0.01$). Micro-CT can quantitatively and sequentially detect murine emphysematous changes, offering a practical method to sequentially analyze the therapeutic effects of treatments in a murine model of emphysema.

Key words emphysema; computed tomography; elastase

Chronic obstructive pulmonary disease (COPD) is one of the serious causative diseases in death of aging people.[1] Emphysema, one of COPD, is characterized as destruction of airway wall and small airway inflammation.[1] An imbalance between elastinolytic proteases and their natural inhibitors is thought to play a role in the pathogenesis of emphysema. One animal model of emphysema is made by administrating of elastase into the lungs.[2—4] Cigarette smoke-induced emphysema is another common model of emphysema. A study of elastase-deficient mice has revealed that elastase is also critical in smoke-induced emphysema.[5] As several months are required to establish cigarette smoke-induced emphysema, the elastase-induced model is more convenient for assessing drug effects.

To quantitatively assess the murine model of emphysema, historical assessment using mean linear intercept (Lm) has been used.[6] Because the elastase-induced destruction of airway wall is not homogenous, random several views are taken to estimate the destruction.

The non-homogenous region of the disease is also applicable for human. In human, noninvasive computed tomography (CT) is commonly used for diagnosis and disease staging by assessing areas of low attenuation.[1,7] The primary benefits of CT monitoring are the ability to assess the lungs in their entirety and the ability to follow the same mice over time.

Micro-computed tomography has been developed, resulting in low-noise CT images in a small animal. CT images are used to follow-up tumor growth in the lung.[8] High respiration rates of mice cause difficulty for high quality of images of the lung. Although invasive methods using tracheostomy enable high quality images,[9,10] we employed free-breathing method to take the images serially in a deeply-anesthetized condition, in which respiration rates were reduced. The purpose of present study is to clarify whether the kinetics of a murine elastase-induced emphysema model can be assessed using CT and to compare the results with morphological analysis.

MATERIALS AND METHODS

Administration of Elastase C57BL/6N mice were obtained from Charles River Japan (Kanagawa, Japan) and bred in the animal facilities of Musashino University School of Medicine under specific pathogen-free (SPF) conditions. Care and use of animals followed the guidelines of the "Principles of Laboratory Animal Care" formulated by the National Society for Medical Research.

Four cycles of sequential CT analysis were performed using 26 mice, six of which were also under histological examination at the end points. For histological analysis only, 12 mice were used for each time points, and in 8 different time points were examined. Another six mice were employed under CT and histological analysis once at the same day.

Mice were anesthetized with ether or intraperitoneal injection of ketamine (90 mg/kg) and xylazine (1 mg/kg) and given intranasal administration of 0.3 or 1.2 units of porcine pancreatic elastase (Sigma-Aldrich, St. Louis, MO, U.S.A.) in 30 μl saline solution. Control mice were intranasally administered saline alone.

CT Assessment After anesthesia was induced with ketamine (90 mg/kg) and xylazine (1 mg/kg), mice were placed in the chamber of the CT scanner for small animal (LaTheta; Aloka, Tokyo, Japan).[9] Anesthesia using ketamine and xylazine induces weak and reduced respiration. The calibration of the CT is conducted using the standard phantom followed by manufacture's instruction. The X-ray intensity and X-ray attenuation are adjusted each time to the level measured at the factory. The X-ray intensity of air is −1000 Hounsfield units (HU) and water is 0 HU. Both X-ray and detector rotated around the mice. The scanning was employed continuously. X-ray was 50 kV with 1 mA s. Scanning time was 4.5 s for one slice. Slice thickness was 0.25 mm. The size of image matrix was 480×480 and the field of view was 48 mm in resolution of 0.10 mm per pixel. Because previous reports have revealed that area of lower than −620 HU are significantly increased in parallel to the degree of emphysematous

* To whom correspondence should be addressed. e-mail: naoyama@musashino-u.ac.jp

lung and set the threshold level as "around −600 HU",[10,11] areas between −800 and −600 HU were recognized as areas of low density for lung field analysis. Total volume of low-density areas in the whole lung was calculated by attached software for measuring area of indicted HU in LaThea.[9] The area of each slice was reconstructed using slice thickness (0.25 mm). Three dimensional analyses were undertaken using software Vgstudio Max (Nihon Visual Science Inc.), using reconstructing images possessing 0.25 mm thickness.

The absorbed radiation dose is 8 mGy per scanning one slice. All mice recovered from anesthesia after several hours. Anesthesia and CT scanning did not influence body weights.

BALF Cell and Histological Examination BALF was obtained from select mice by incubating and washing the lung with 1 ml of saline each time. We repeated BAL until the recovered volume was 5 ml. BALF was centrifuged at 1500 rpm for 10 min at 4 °C. Pellets were resuspended in 1 ml PBS and the number of cells was counted. Cytospin specimens were obtained by centrifugation at 640 rpm for 2 min. Cytospin slides were stained with Diff Quik (International Reagents Corporation) and the cell fractions were examined by microscope.

For histological analysis, the lungs were inflated and fixed by intratracheal administration of 10% formalin at a constant pressure of 25 cmH_2O. The lung was serially divided into transverse section as CT scan and embedded by paraffin. Specimens stained with hematoxylin and eosin (HE) were assessed by analyzing Lm, as determined on random 20 photomicroscopic images per animal.[6,12] Photomicroscopic images were taken using Digital sight (Nikon, Kanagawa, Japan).

To measure intercept, horizontal and vertical lines were drawn in the images. Intercepts of alveolar walls with these lines were counted and length of mean linear intercept was estimated.

RNA Extraction and Quantification of mRNAs Lungs were frozen in liquid nitrogen immediately after isolation and were used for RNA extraction. Lung tissue was homogenized at 4 °C and total RNA was extracted using ISOGEN, which is a modified acid guanidium–phenol–chloroform method (Nippon Gene Co., Ltd., Tokyo, Japan). RNA was treated with 10u DNase (Qiagen, Hiden, Germany) following manufacturer's instruction. The purity of the RNA was established by spectrophotometer using a DNA purity calculating program (Hitachi Seisakusho, Tokyo, Japan). The absorbance OD260/280 ratio was 1.8. After the amount of total RNA was measured, cDNA synthesis was performed with 0.125 μM oligo-dT (Takara Biochemicals, Tokyo, Japan) as previously described.[13] The levels of mRNA were examined by real-time PCR using the Light Cycler-Fast Start DNA Master Syber GreenI kit (Roche Diagnostics, Mannheim, Germany). In this system, double-stranded DNA is labelled with Syber Green I and then detected. Quantification was performed on the basis of the standard curve obtained using serial dilution of specific PCR products. To produce specific PCR products, cDNA were amplified by 35 cycles (30 s at 95 °C, 30 s at 58 °C, 30 s at 72 °C), using specific primer and *taq* polymerase. Initial denaturation step was 2 min at 95 °C and final extension period was 5 min at 72 °C. PCR products were then electrophoresed using 2% agarose gel with ethidium bromide, followed by purification using QIAquick Gel Extraction kit (Qiagen).

Results of real time PCR are shown as ratios of the level of mRNAs standardized by the level of β-actin mRNA.

The primers used were as follows; β-actin 5′-CCTGTATGCCTCTGGTCGTA-3′ 5′-CCATCTCCTGCTCGAAGTCT-3′ 260 bp, TNF-α 5′-CAGACCCTCACACTCAGATCA-3′ 5′-GTCCCTTGAAGAGAACCTGG-3′.

Statistics For comparisons of multiple parameters, we used Wilxon's rank-sum tests or Mann–Whitney's U test. Data are expressed as mean±standard deviation of the mean (S.D.). The coefficient of correlation was evaluated using Spearman's correlation coefficient by rank. The level of statistical significance was set at $p<0.05$.

RESULTS

Time Course Assessment of Inflammation Induced by Elastase After elastase administration, significant neutrophil accumulation was observed on day 1 ($p<0.05$) (Fig. 1A). This inflammation was resolved by 1 week. The cytokine mRNA expression was also examined at the same

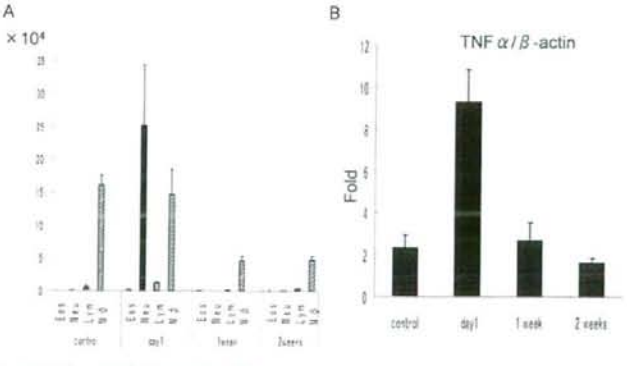

Fig. 1. BALF Cell Analysis (A) and TNF-α mRNA Expression (B)

(A) BALF cells were placed on glass slides using Cytospin. Slides were then stained with Diff Quik, and cell differentiation was assessed microscopically. The ordinate exhibited the number of cells in total BALF (5 ml). Each bar indicates means±S.D. of five different mice. (B) TNF-α mRNA expression was determined by real-time PCR. RNA was extracted from whole lung. The ordinate indicated the mRNA expression compared the standardized level of β-actin mRNA. Data are mean±S.D. of four different mice.

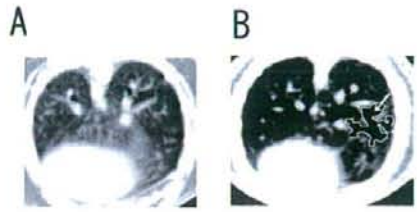

Fig. 2. CT Images for Saline-Treated Mice (A) and Elastase-Treated Mice (B)

Example of low density area −800 and −600 HU is shown by arrow in (B).

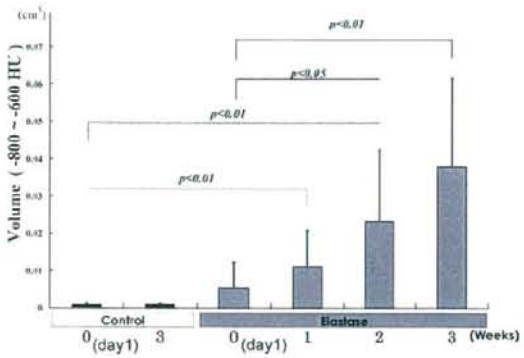

Fig. 3. Sequential Quantification by CT

Areas of lung between −800 and −600 HU were recognized as low-density areas. Total volume of low-density areas was calculated. The trachea and artifacts were removed from calculations. Each bar represents mean±S.D. of values obtained from 6–11 mice.

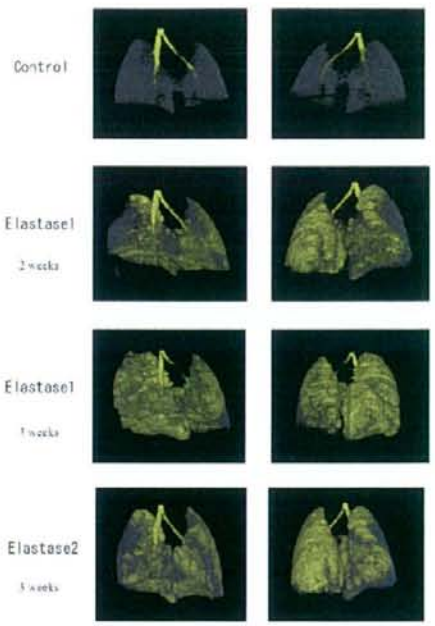

Fig. 4. Three-Dimensional Reconstructions of CT

Yellow areas indicate −800 to −600 HU. Although the trachea and bronchi are shown as yellow areas in this figure, the trachea and bronchi were removed from calculations. The density of trachea and bronchi was about −900, which was lower than that of the lung. If these areas were included, low density areas were overestimated. Elastase 1 at 2 and 3 weeks are from the same mice. Elastase 1 and Elastase 2 are for different animals treated with elastase in exactly the same manner. Left panel is shown from the front and right panel is from the back of the same mice.

time. TNF-α, which is ascribed one of the causative cytokines of emphysema, was significantly increased on day 1 and returned to baseline by 1 week ($p<0.01$) (Fig. 1B).

Time Course Assessment of Air Wall Destruction Using CT and Morphometry Elastase-treated mice (Fig. 2B) exhibited a low-density area compared to controls (Fig. 2A). Next, we sequentially analyzed the same mice once a week after administration of elastase (0.3 units), using CT (Fig. 3). For quantitative assessments, areas from −800 to −600 HU were accumulated and showed as volume of low density lung. Volume of low density area for elastase treated mice was $0.01118\pm0.00968\,cm^3$, significantly greater than that of control mice ($0.00096\pm0.00034\,cm^3$) ($n=11$ each group, $p<0.01$), but not statistically significant compared with elastase treated mice Day 1. At 2 weeks, a significant increase in total volume of low-density areas was observed compared with control mice and elastase-treated mice Day 1 ($p<0.01$ and $p<0.05$, respectively), and a further increase was observed at 3 weeks (Fig. 3).

To obtain whole lung images by CT scanning, 3-dimensional reconstruction was performed using software Vgstudio Max (Fig. 4). This revealed an expanding pattern of lung destruction from 2 to 3 weeks (Fig. 4). This analysis also showed that low density lesions were not homogenous and that differences existed in areas of lung destruction (Fig. 4).

To compare time-course analysis of CT with previous methods, histological examination was performed. For histological time-course analysis, mice had to be sacrificed at each time point ($n=6$ in each time point). All mice were treated in the same manner as mice in Fig. 2. Histological analysis revealed destruction of the lung from day 1 (Fig. 5). Lung destruction continued to 3 weeks (Fig. 4). Lm was calculated to estimate alveolar wall destruction, as this is the most commonly used method to assess emphysematous lungs. Significant increases in Lm were observed at 1 week

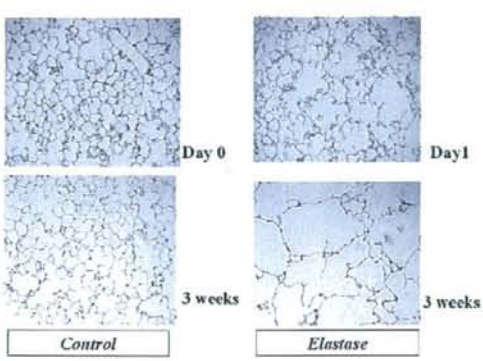

Fig. 5. Histological Analyses by HE Staining

Mice were sacrificed at the day indicted after administration of elastase or saline. Lungs were slowly inflated using 25 cmH_2O pressures to avoid further damage to the lungs. Original magnification ×200.

($p<0.05$; Fig. 6), earlier than the CT evaluation. Control mice did not exhibit any changes during experiments.

After 6 months, 3 elastase-treated mice (same mice in Fig. 3) were examined by CT to obtain follow-up images. Mean volume of accumulated low-density area on CT at 6 months was $0.08\pm0.0127\,cm^3$, significantly greater than that at 3 weeks ($p<0.01$), suggesting that destruction of alveolar walls had not recovered. Mean Lm for these mice was $52.0\pm5.2\,\mu m$, significantly greater than that of control mice ($28.1\pm0.5\,\mu m$).

Direct Comparison of CT and Morphometry To clarify correlations between CT and Lm, we analyzed CT results and morphometry using the same mice at the same time. To obtain severe destruction, we used 1.2 units of elastase and shook the mice after elastase administration. This method allowed us to obtain the ratio of destroyed lung to whole lung, reaching $55.6\pm5.2\%$ at 3 weeks. Both the percentage of the low-density area (A) and the mean CT level (B) significantly correlated with Lm (Fig. 7). Coefficients of correlation were 0.80 and 0.85, respectively ($p<0.01$ each).

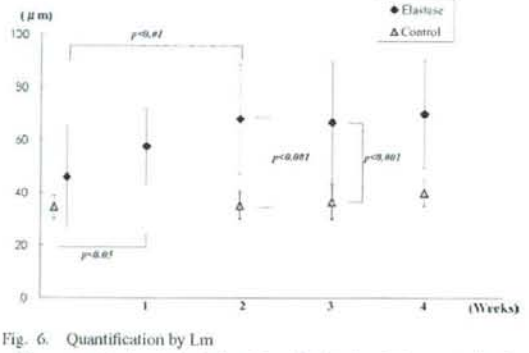

Fig. 6. Quantification by Lm

Mice was sacrificed at the day indicted after administration of elastase or saline. Lm was determined on 20—30 photomicroscopic images per HE-stained specimen. The value of Lm was showed in ordinate. Each bar represents mean±S.D. of values obtained from 4 different mice.

DISCUSSION

In the present study, we quantified the kinetics of murine elastase-induced emphysema model by computed tomography, and compared the results with morphological analysis. The primary benefits of CT monitoring are the ability to assess the lungs in their entirety and the ability to follow the same mice over time. Our data demonstrate that CT can detect emphysematous changes in the elastase treated lung, comparable to morphological analysis by measuring Lm. CT images obtained from anesthetized mice could not detect alveolar destruction earlier than morphometric analysis, but had the advantage of allowing the same mouse to be measured sequentially and quantitatively. As intranasal administration of elastase does not damage the lung homogeneously, sequential whole-lung analyses provide more accurate quantification.

Elastase activates protease-activated receptor-2, resulting inflammatory mediator synthesis and neutrophil influx.[14—16] The both neutrophil and macrophages are proposed to play a critical role in the pathogenesis of emphysema in human and animal models.[1,3,17] Among inflammatory cytokines, TNF-α is known as a most causative one, which is produced by macrophages and epithelial cells.[17] In elastase-induced model in our experiments, both influx of neutrophil and upregulation of TNF-α mRNA were observed and retuned to normal level by 1 week. Further destruction of airway wall is partly attributable to mechanical stress.[2,11]

In humans, noninvasive CT follow-up is a common procedure to assess emphysema.[7,18] In the murine model, quantitative analysis is commonly undertaken by measuring Lm on formalin-fixed specimens. This method of quantifying Lm is authorized,[6] but cannot estimate the whole lung. Micro-CT has become available to assess various animal models. Micro-CT has also been applied to assess pulmonary fibrosis and metastatic lung cancer.[8,19,20] The high respiration rate of mice forces using fixed lung or tracheostomized and breath fold lung for precise analysis, resulting in visualization of alveoli and estimation pulmonary function even in small animals.[10,11,21,22] Recently respiratory-gating methods is developed and provide clearer vision to estimate even airway diameter.[23] The micro-CT, which we used in this manuscript,

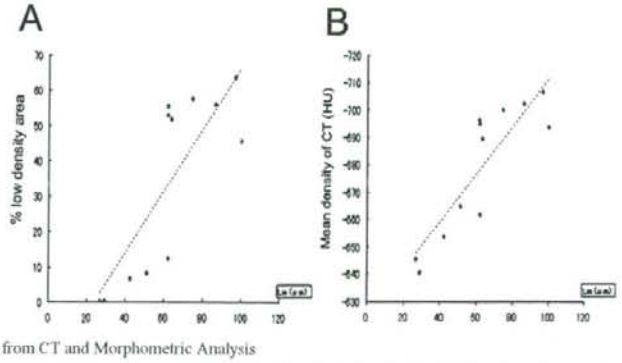

Fig. 7. Comparison of Results from CT and Morphometric Analysis

Correlations between CT and Lm were analyzed using mice with several levels of lung destruction ($n=12$). (A) Percentage of low-density area compared to total lung volume as determined by CT (y-axis) and Lm (x-axis). The coefficient of correlation is 0.79 ($p<0.01$). (B) Mean density of CT (HU) (y-axis) and Lm (x-axis). The coefficient of correlation is 0.85 ($p<0.001$).

has been used for quantifying fat volume and bone mineral density.[24—26] In order to assess mice sequentially, we used deep anesthetized mice, which have been previously reported to deserve for evaluation.[7,19,20] Although artifacts due to respiratory movement could not be eliminated in our study and areas of low density may have been slightly underestimated, we found that it is applicable to the sequential estimation of detecting murine emphysematous lung. By using the software contained in CT apparatus, which has been validated for quantifying fat volume and bone mineral density,[24—26] low density area was calculated and the value exhibited good correlation to the value estimated by Lm. The absorbed radiation dose is 8 mGy per scanning one slice, which is relatively lower compared to other micro-CT and not lethal level.[27,28]

For human low attenuation area was determined as lower −900 HU.[9,18] However, studies reveal lowest value is −800 HU and never reached −950 HU in murine emphysematous lung.[29,30] In addition, mean density of murine normal lung is around −500 to −600 HU by ours and Plathow *et al.*[20] and around −400 HU,[20,29,30] which is quite different from that of human (−700 HU).[7,18] Therefore, we used the level between −800 and −600 HU for estimating low density area in a murine model.

The estimation of low density area of our study was comparable to previous reports, although CT apparatus and method of anesthesia are different.[29,30] Froese *et al.* used knockout mice which develop emphysema spontaneously, resulting that correlation of morphology to CT densities was r^2 of 0.53. Pastnov *et al.* have shown possibility of assessment of elastase-induced emphysema in murine model, but the lung was examined once on day 14.[29] In this report, we showed usefulness of sequential quantitative analysis. We were able to detect sequential increases in tissue destruction in the same area of the lung using CT images. In addition, these data correlated well with morphometric analyses using Lm (r^2 of 0.72, Fig. 7B). As alveolar wall destruction was not heterogeneous, evaluation of the whole lung is worthwhile in this emphysema model. Micro-CT is expected to provide a practical method for sequential analysis of therapeutic effects in a murine model of emphysema.

Acknowledgements This study was supported in part by a High-Tech Research Center Grant from Science and Technology (No. 13670473 for Musashino University) and Grants-in-Aid for Scientific Research from the Ministry of Education, Culture, Sports, Science and Technology of Japan.

REFERENCES

1) Rabe K. F., Hurd S., Anzueto A., Barnes P. J., Buist S. A., Calverley P., Fukuchi Y., Jenkins C., Rodriguez-Roisin R., van Weel C., Zielinski J., *Am. J. Respir. Crit. Care Med.*, **176**, 532—555 (2007).
2) Lucey E. C., Goldstein R. H., Stone P. J., Snider G. L., *Am. J. Respir. Crit. Care Med.*, **158**, 555—564 (1998).
3) Shapiro S. D., Ingenito E. P., *Am. J. Respir. Cell Mol. Biol.*, **32**, 367—372 (2005).
4) Snider G. L., Lucey E. C., Stone P. J., *Am. Rev. Respir. Dis.*, **133**, 149—169 (1986).
5) Shapiro S. D., Goldstein N. M., Houghton A. M., Kobayashi D. K., Kelley D., Belaaouaj A., *Am. J. Pathol.*, **163**, 2329—2335 (2003).
6) Thurlbeck W. M., *Am. Rev. Respir. Dis.*, **95**, 752—764 (1967).
7) Parr D. G., Dawkins P. A., Stockley R. A., *Am. J. Respir. Crit. Care Med.*, **174**, 954—955 (2006).
8) De Clerck N. M., Meurrens K., Weiler H., Van Dyck D., Van Houtte G., Terpstra P., Postnov A. A., *Neoplasia*, **6**, 374—379 (2004).
9) Kanazawa S., Ota S., Sekine C., Tada T., Otsuka T., Okamoto T., Sonderstrup G., Peterlin B. M., *Proc. Natl. Acad. Sci. U.S.A.*, **103**, 14465—14470 (2006).
10) Litzlbauer H. D., Neuhaeuser C., Moell A., Greschus S., Breithecker A., Franke F. E., Kummer W., Rau W. S., *Am. J. Physiol. Lung Cell Mol. Physiol.*, **291**, L535—L545 (2006).
11) Sera T., Uesugi K., Yagi N., *J. Physiol. Anthropol. Appl. Human Sci.*, **24**, 465—468 (2005).
12) Robbesom A. A., Versteeg E. M., Veerkamp J. H., van Krieken J. H., Bulten H. J., Smits H. T., Willems L. N., van Herwaarden C. L., Dekhuijzen P. N., van Kuppevelt T. H., *Mod. Pathol.*, **16**, 1—7 (2003).
13) Yamashita N., Tashimo H., Ishida H., Matsuo Y., Tamauchi H., Terashima M., Yoshiwara I., Habu S., Ohta K., *Am. J. Physiol. Lung Cell Mol. Physiol.*, **290**, L1045—L1051 (2006).
14) Domotor E., Bartha K., Machovich R., Adam-Vizi V., *J. Neurochem.*, **80**, 746—754 (2002).
15) Dulon S., Cande C., Bunnett N. W., Hollenberg M. D., Chignard M., Pidard D., *Am. J. Respir. Cell Mol. Biol.*, **28**, 339—346 (2003).
16) Uehara A., Muramoto K., Takada H., Sugawara S., *J. Immunol.*, **170**, 5690—5696 (2003).
17) Chung K. F., *Curr. Drug Targets Inflamm. Allergy*, **4**, 619—625 (2005).
18) Coxson H. O., *Eur. Respir. J.*, **29**, 1075—1077 (2007).
19) Greschus S., Kiessling F., Lichy M. P., Moll J., Mueller M. M., Savai R., Rose F., Ruppert C., Gunther A., Luecke M., Fusenig N. E., Semmler W., Traupe H., *Neoplasia*, **7**, 730—740 (2005).
20) Plathow C., Li M., Gong P., Zieher H., Kiessling F., Peschke P., Kauczor H. U., Abdollahi A., Huber P. E., *Invest. Radiol.*, **39**, 600—609 (2004).
21) Sera T., Uesugi K., Yagi N., *Respir. Physiol. Neurobiol.*, **147**, 51—63 (2005).
22) Onclinx C., De Maertelaer V., Gustin P., Gevenois P. A., *Radiology*, **241**, 763—770 (2006).
23) Ford N. L., Martin E. L., Lewis J. F., Veldhuizen R. A., Drangova M., Holdsworth D. W., *J. Appl. Physiol.*, **102**, 2046—2055 (2007).
24) Iwakura H., Hosoda K., Son C., Fujikura J., Tomita T., Noguchi M., Ariyasu H., Takaya K., Masuzaki H., Ogawa Y., Hayashi T., Inoue G., Akamizu T., Hosoda H., Kojima M., Itoh H., Toyokuni S., Kangawa K., Nakao K., *J. Biol. Chem.*, **280**, 15247—15256 (2005).
25) Oike Y., Akao M., Yasunaga K., Yamauchi T., Morisada T., Ito Y., Urano T., Kimura Y., Kubota Y., Maekawa H., Miyamoto T., Miyata K., Matsumoto S., Sakai J., Nakagata N., Takeya M., Koseki H., Ogawa Y., Kadowaki T., Suda T., *Nat. Med.*, **11**, 400—408 (2005).
26) Shimada T., Yamazaki Y., Takahashi M., Hasegawa H., Urakawa I., Oshima T., Ono K., Kakitani M., Tomizuka K., Fujita T., Fukumoto S., Yamashita T., *Am. J. Physiol. Renal. Physiol.*, **289**, F1088—F1095 (2005).
27) Carlson S. K., Classic K. L., Bender C. E., Russell S. J., *Mol. Imaging Biol.*, **9**, 78—82 (2007).
28) Ford N. L., Thornton M. M., Holdsworth D. W., *Med. Phys.*, **30**, 2869—2877 (2003).
29) Postnov A. A., Meurrens K., Weiler H., Van Dyck D., Xu H., Terpstra P., De Clerck N. M., *J. Microsc.*, **220**, 70—75 (2005).
30) Froese A. R., Ask K., Labiris R., Farncombe T., Warburton D., Inman M. D., Gauldie J., Kolb M., *Eur. Respir. J.*, **30**, 1082—1089 (2007).

Am J Physiol Renal Physiol 294: F542–F553, 2008.
First published January 2, 2008; doi:10.1152/ajprenal.00201.2007.

Multiple renal cysts, urinary concentration defects, and pulmonary emphysematous changes in mice lacking TAZ

Ryosuke Makita,[1,2] Yasunobu Uchijima,[1] Koichi Nishiyama,[1] Tomokazu Amano,[2] Qin Chen,[3] Takumi Takeuchi,[3] Akihisa Mitani,[1,4] Takahide Nagase,[4] Yutaka Yatomi,[5] Hiroyuki Aburatani,[6] Osamu Nakagawa,[7,8] Erin V. Small,[7] Patricia Cobo-Stark,[9] Peter Igarashi,[9] Masao Murakami,[1,10] Junji Tominaga,[1] Takahiro Sato,[1] Tomoichiro Asano,[1,11] Yukiko Kurihara,[1] and Hiroki Kurihara[1]

Departments of [1]Physiological Chemistry and Metabolism, [2]Developmental Medical Technology (Sankyo), [3]Urology, [4]Respiratory Medicine, and [5]Laboratory Medicine, Graduate School of Medicine and [6]Genome Science Division, Research Center for Advanced Science and Technology, The University of Tokyo, Tokyo; [10]Department of Medicine and Clinical Science, Kyoto University Graduate School of Medicine, Kyoto; [11]Department of Biomedical Chemistry, Hiroshima University Graduate School of Biomedical Sciences, Hiroshima, Japan; and [7]Division of Cardiology, Departments of Internal Medicine, [8]Molecular Biology, and [9]Internal Medicine and Pediatrics, The University of Texas Southwestern Medical Center at Dallas, Dallas, Texas

Submitted 28 April 2007; accepted in final form 31 December 2007

Makita R, Uchijima Y, Nishiyama K, Amano T, Chen Q, Takeuchi T, Mitani A, Nagase T, Yatomi Y, Aburatani H, Nakagawa O, Small EV, Cobo-Stark P, Igarashi P, Murakami M, Tominaga J, Sato T, Asano T, Kurihara Y, Kurihara H. Multiple renal cysts, urinary concentration defects, and pulmonary emphysematous changes in mice lacking TAZ. *Am J Physiol Renal Physiol* 294: F542–F553, 2008. First published January 2, 2008; doi:10.1152/ajprenal.00201.2007.— TAZ (transcriptional coactivator with PDZ-binding motif), also called WWTR1 (WW domain containing transcription regulator 1), is a 14-3-3-binding molecule homologous to Yes-associated protein. TAZ acts as a coactivator for several transcription factors as well as a modulator of membrane-associated PDZ domain-containing proteins, but its (patho)physiological roles remain unknown. Here we show that gene inactivation of TAZ in mice resulted in pathological changes in the kidney and lung that resemble the common human diseases polycystic kidney disease and pulmonary emphysema. *Taz*-null/*lacZ* knockin mutant homozygotes demonstrated renal cyst formation as early as *embryonic day 15.5* with dilatation of Bowman's capsules and proximal tubules, followed by pelvic dilatation and hydronephrosis. After birth, only one-fifth of TAZ-deficient homozygotes grew to adulthood and demonstrated multicystic kidneys with severe urinary concentrating defects and polyuria. Furthermore, adult TAZ-deficient homozygotes exhibited diffuse emphysematous changes in the lung. Thus TAZ is essential for developmental mechanisms involved in kidney and lung organogenesis, whose disturbance may lead to the pathogenesis of common human diseases.

renal disease; knockout mice; transcription factor

TAZ (TRANSCRIPTIONAL COACTIVATOR with PDZ-binding motif), also called WWTR1 (WW domain containing transcription regulator 1), is a 14-3-3-binding molecule homologous to Yes-associated protein (YAP) (14, 18). TAZ, as well as YAP, possess a WW domain that can bind to the PPXY motif present in some transcription factors. Through this interaction and additional unknown mechanisms, TAZ can act as a coactivator for several transcription factors, including Runx2/Cbfa1, TTF-1/Nkx2.1, Tbx5, and Pax3 (5, 24, 25, 30). The COOH-terminal region of TAZ contains a PSD-95, Dlg, and ZO-1 homology (PDZ)-binding motif that localizes TAZ to discrete foci in the nucleus and is essential for its activity as a transcriptional coactivator (18). TAZ and YAP also bind to membrane-associated PDZ domain-containing proteins through this motif. In particular, TAZ and YAP bind to sodium/hydrogen exchanger regulatory factor (NHERF)-2 and NHERF, respectively, which may link TAZ and YAP to transmembrane receptors and actin-binding proteins (14, 18). Furthermore, a recent report demonstrated that TAZ may modulate mesenchymal stem cell differentiation into osteogenic and adipogenic lineages by coactivating Runx2/Cbfa1 and repressing peroxisome proliferator-activated receptor-γ-dependent gene transcription (13). Thus TAZ and YAP are now regarded as context-dependent transcriptional modulators in various cell types that may link events at the plasma membrane and cytoskeleton to nuclear transcription, possibly in a 14-3-3-dependent manner (14, 18).

In midgestation mouse embryos, TAZ is mainly expressed in the paraxial mesoderm, limb buds, and the neural tube (25). Later, TAZ is distributed more broadly in various tissues and organs (18 and UniGene's EST ProfileViewer). The broad distribution of TAZ and its interaction with different transcription factors essential for embryonic development led us to investigate the physiological role of TAZ by a gene targeting strategy.

Here, we demonstrate that inactivation of the mouse *Taz* gene in mice results in the formation of multiple cysts in the kidney and greatly enlarged air spaces in the lung. These phenotypes resemble human polycystic kidney diseases (PKD) and pulmonary emphysema, respectively. PKD is a human inherited renal disorder that is the most common genetic cause of renal failure in children and adults (3, 15). Autosomal dominant polycystic kidney disease (ADPKD) is the most prevalent form, with an incidence of 1–2 per 1,000 individuals and is characterized by bilateral formation of multiple cysts arising from any segment of the nephrons and collecting ducts. ADPKD is caused by mutations in either of two genes, *PKD1*

Address for reprint requests and other correspondence: H. Kurihara, Dept. of Physiological Chemistry and Metabolism, Graduate School of Medicine, Univ. of Tokyo, 7-3-1 Hongo, Bunkyo-ku, Tokyo 113-0033, Japan (e-mail: kuri-tky@umin.ac.jp).

The costs of publication of this article were defrayed in part by the payment of page charges. The article must therefore be hereby marked "*advertisement*" in accordance with 18 U.S.C. Section 1734 solely to indicate this fact.

and *PKD2*, that encode membrane-associated proteins polycystin-1 and polycystin-2, respectively (23, 32, 33). Autosomal recessive polycystic kidney disease (ARPKD) is much less frequent (1/20,000 live births) and is caused by mutations of *PKHD1* (29, 37), which encodes polyductin/fibrocystin, a large transmembrane protein. Although the causative genes have been identified, the molecular mechanism underlying cystic formation remains largely unknown.

TAZ-deficient mice also exhibited urinary concentration defects, polyuria, and hydronephrosis. Although urinary concentrating defects have been observed in human ADPKD and ARPKD, massive polyuria and hydronephrosis are uncommon. These findings suggest that the pathophysiological processes in TAZ-deficient kidneys and human PKD are different in some respects. The similarities and dissimilarities between TAZ-deficient mice and PKD may provide important clues to understanding the pathogenesis of a common human disease.

In addition, the dilatation of air spaces of the lung in TAZ-deficient mice is morphologically reminiscent of human pulmonary emphysema, which is a common disease that causes death and disability, especially in the aged (1, 12). As a manifestation of chronic obstructive pulmonary disease (COPD), pulmonary emphysema is characterized by enlargement of air spaces and destruction of the alveolar wall. Although α-antitrypsin deficiency is known to cause a congenital form of pulmonary emphysema, little remains known concerning the molecular mechanisms underlying the pathogenesis of this disease. TAZ-deficient mice may also serve as a novel animal model for COPD as well as kidney diseases.

MATERIALS AND METHODS

Generation and genotyping of mutant mice. A C57BL6/J-derived BAC clone containing the mouse *Taz* gene was obtained from BACPAC Resource Center (Oakland, CA). The *nls-lacZ/PGKneo* cassette was made by placing the *lacZ* gene with a nuclear localization signal (*nls-lacZ*) adjacent to the *PGKneo* gene and flanking it with *lox71* at the 5′-end and *lox2272* at the 3′-end to allow recombinase-mediated cassette exchange. A pKO Scrambler NTKV-1904 plasmid (Stratagene) was used as a backbone vector. For the targeting construct, a PCR-amplified 1.2-kb fragment extending from the promoter region to the 5′-untranslated region in exon 2 and an 8.2-kb *Ngo*MIV-*Bam*HI fragment from intron 2 were inserted on each side of the *nls-lacZ/PGKneo* cassette (Fig. 1*A*). The targeting vector was linearized and electroporated into the B6129F1-derived embryonic stem (ES) cell line ATOM1 (Amano T et al., unpublished observations).

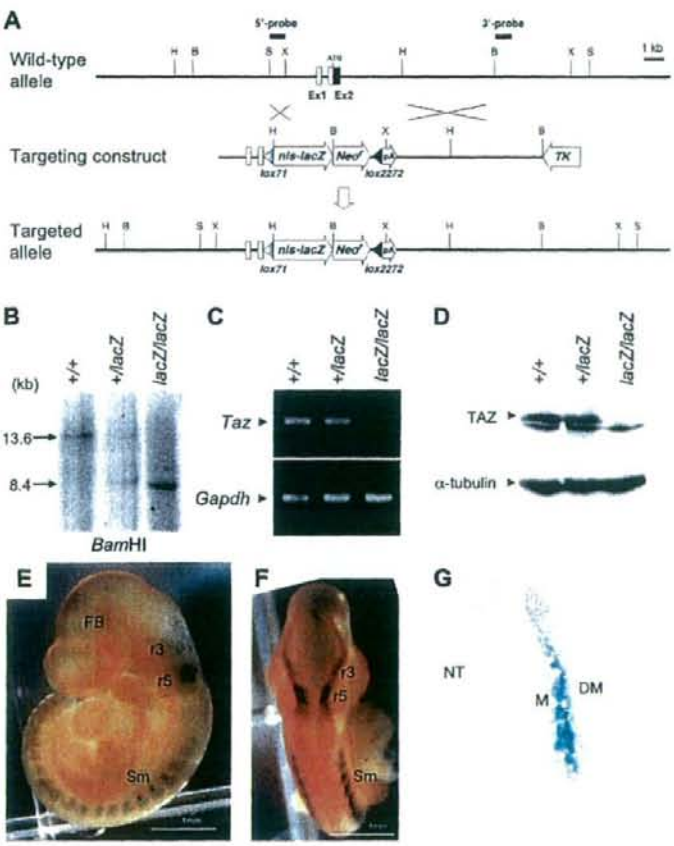

Fig. 1. Targeting of the mouse *Taz* (transcriptional coactivator with PDZ-binding motif) gene. *A*: schematic representation of the targeting strategy employed to knockin an *nls-lacZ* cassette into the *Taz* locus. Two different probes for genotyping are indicated as 5′- and 3′-probes. B, *Bam*HI; H, *Hind*III; S, *Sful*; X, *Xba*I. *B*: representative genotyping of the offspring from an F_1 intercross by Southern blot analysis. Genomic DNA samples were digested with *Bam*HI and probed with the 5′-probe. Bands of 13.6 and 8.4 kb represent wild-type and mutant alleles, respectively. *C* and *D*: RT-PCR (*C*) and Western blot (*D*) confirming the absence of TAZ expression in $Taz^{lacZ/lacZ}$ embryos. Total RNA and protein extracts were obtained from *embryonic day 15.5* whole embryos. Lower band in *D*, *top*, represents nonspecific binding. *E–G*: lateral (*E*) and dorsal (*F*) views of an *embryonic day 9.5* $Taz^{+/lacZ}$ embryo and a section at the level of the somites (*G*) stained with X-gal. FB, forebrain; DM, dermomyotome; M, myotome; NT, neural tube; r3 and r5, rhombomeres 3 and 5 of the hindbrain; Sm, somites.

Clones that survived positive-negative selection with neomycin and 1-(2′-deoxy-2′-fluoro-1-β-D-arabinofuranosyl)-5-iodouracil were screened for homologous recombination with diagnostic PCR primers. Targeted clones were injected in ICR blastocysts to generate germline chimeras. Mice homozygous for the Taz^{lacZ} allele were obtained by intercrossing F_1 heterozygotes. The genotypes of the offspring were determined by PCR or Southern blot analysis on tail-tip or amnion DNA. All animal experiments were reviewed and approved by the University of Tokyo Animal Care and Use Committee.

RT-PCR. Total RNA was extracted using ISOGEN (Nippon Gene). The reverse transcription reaction was carried out using SuperScriptIII (Invitrogen). PCR was then performed on the resulting cDNA using the primers 5′-GAAAATCACCACATGGCAAGACCC-3′ and 5′-TTACAGCCAGGTTAGAAAGGGCTC-3′ for *TAZ* (product size, 748 bp; annealing, 64°C), 5′-GGCTATGTGCAGTGTCATGTC-3′ and 5′-CTGTGATATGCCAGTGGTCAG-3′ for *Aqp1* (product size, 462 bp; annealing, 58°C), 5′-TGGATTCATGGAGCAGCCCGGT-3′ and 5′-TCCTTCCTTCGAGCTGCCTTC-3′ for*Aqp2* (product size, 312 bp; annealing, 58°C), 5′-ATCAAGCTGCCCATCTACAC-3′ and 5′-GGGCCAGCTTCACATTCTC-3′ for *Aqp3* (product size, 559 bp; annealing, 56°C), and 5′-GGTGTGAACCACGAGAAATAT-3′ and 5′-AGATCCACGACGGACACATT-3′ for *Gapdh* (product size, 335 bp; annealing, 56°C). For comparison of *Pkd1*, *Pkd2*, and *Pkhd1* expression levels, quantitative real-time RT-PCR was performed using the LightCycler system (Roche diagnostics) according to the manufacturer's protocol. Sequences of the primers were as follows; 5′-GGATGGTGATCAGACACCGCTCAA-3′ and 5′-TTGGTGGCTTCTTCCTTCCGACCT-3′ for *Pkd1*, 5′-TCTCCTCAGGTTATTGGCGGAGTT-3′ and 5′-GACATAGCGGATCAGTTTTACAGG-3′ for *Pkd2*, 5′-GGCGCCACAGACAAACAATTA-3′ and 5′-GCCCTGCAGTTCTAGCTTGGTT-3′ for *Pkhd1*, and 5′-GGTTGGCCCTGGGAGTACCAAGAA-3′ and 5′-AATGGGAAGCCCAAGTGCCTCTGT-3′ for *Avpr2*.

Western blotting. Anti-TAZ rabbit polyclonal antibody was previously described (25). Western blotting was performed on lysates from *embryonic day 13.5* whole embryos or 12-wk-old kidneys using a standard protocol.

Histology. For histological analysis, samples were fixed in formalin, embedded in paraffin, cut into 2-μm-thick sections, and stained with hematoxylin and eosin. Photomicrographs were obtained using a computer-assisted microscope (Nikon ECLIPSE 80i).

Urinary analysis. Urine volume was measured using the 48-h frequency/volume analysis system as previously described (4). Briefly, each mouse was placed in a metabolic cage connected to a digital scale and personal computer. Each mouse was provided with free access to food and water. After mice were acclimatized for 2 days in the cage, water intake, urine voiding frequency, and volume per void were recorded for 48 h.

Lectin and immunofluorescent staining. Lectin staining was performed on cryosectioned kidneys. *Embryonic day 18.5* kidneys were dissected, embedded in optimum-cutting temperature (OCT) compound (Miles), and cut into 10-μm-thick sections. After being blocked with blocking buffer, the sections were incubated for 1 h at 37°C with 20 μg/ml biotin-conjugated *Dolichos biflorus* agglutinin (DBA) or *Lotus tetragonolobus* agglutinin (LTA) followed by extensive washing with blocking buffer. Lectin staining was visualized by reacting with fluorescein isothiocyanate-conjugated streptavidin, and nuclei were counterstained with propidium iodide. Photomicrographs were obtained using a computer-assisted confocal microscope (Nikon D-ECLIPSE C1).

For immunofluorescent staining, paraformaldehyde-fixed cryosections were stained with antibodies to aquaporin-2 (gift from M. Knepper, National Heart, Lung, and Blood Institute, Bethesda, MD) or aquaporin-3 (Chemicon), as described previously (31). Nuclei were stained with 4′,6-diamidine-2-phenylindole (DAPI).

In situ hybridization. Isotopic in situ hybridization was performed on paraffin-embedded sections of *embryonic day 14.5* and *16.5* embryos using ^{35}S-radiolabeled RNA probes for *Taz/Wwtr1* as previously described (27).

β-Galactosidase staining. LacZ expression was detected by staining with X-gal (5-bromo-4-chloro-3-indoyl β-D-galactoside). Staining was performed as described by Nagy et al. (26) with minor modifications. Whole embryos and kidneys were washed in ice-cold PBS containing 2 mM $MgCl_2$ and fixed in 0.1 M phosphate buffer (pH 7.3) containing 0.2% glutaraldehyde, 5 mM EGTA, and 2 mM $MgCl_2$. Following rinsing three times with 0.1 M phosphate buffer containing 2 mM $MgCl_2$, 0.02% Nonidet P-40, 0.01% sodium deoxycholate, and 5 mM EGTA (washing buffer), samples were embedded in OCT compound and cryosectioned. Embryos or sections were incubated overnight at 37°C in X-gal-staining buffer (10 mM potassium ferrocyanide, 10 mM potassium ferricyanide and 2 mg/ml X-gal in washing buffer). For costaining with platelet/endothelial cell adhesion molecule, X-gal-stained sections were rinsed with PBS, incubated in the blocking buffer (see *Lectin and immunofluorescent staining*), and reacted with anti-CD31 antibody (BD Bioscience) (1:100) at 4°C overnight. Immunoreactivity was visualized with the VECTASTAIN ABC kit (Vector laboratories). Sections were counterstained with 1% Orange G (Sigma).

Morphometric analysis. The mean linear intercept, as a measure of interalveolar wall distance, was determined as described by Thurlbeck (34). Briefly, lines were drawn across light microscopic images of the lung section stained with hematoxylin and eosin. The mean linear intercept was calculated by dividing the total length of a line by the total number of intercepts encountered in 72 lines/lung.

Statistical analysis. Mann-Whitney nonparametric test was used to compare values between two groups for morphometric analysis. Student's *t*-test was used for the comparison of values in other experiments. Data were represented as means ± SD. Values of $P < 0.05$ were considered significant.

RESULTS

Generation of Taz-lacZ knockin mice. We disrupted the mouse *Taz* locus by replacing the coding region in exon 2 with an *nls-lacZ/PGKneo* cassette (Fig. 1*A*). Of 683 ES cell clones screened, three clones were positive for the mutant Taz^{lacZ} allele. All three clones were injected in ICR blastocysts and gave rise to male germline chimeras, which were subsequently bred with ICR females to produce $Taz^{+/lacZ}$ heterozygous mice. The heterozygous mice appeared normal and were fertile. Offspring from $Taz^{+/lacZ}$ intercrosses were genotyped by Southern analysis of tail genomic DNA (Fig. 1*B*). The absence of *Taz* transcripts and protein in $Taz^{lacZ/lacZ}$ homozygous mice was confirmed by RT-PCR and Western blotting, respectively (Fig. 1, *C* and *D*).

To verify that *Taz*-directed *lacZ* expression reflected the pattern of authentic *Taz* expression, we stained for *lacZ* in

Table 1. *Genotypic distribution of offspring from heterozygous matings*

Age	Wild-type	*Taz/lacZ/+*	*Taz/lacZ/lacZ*	Total
E8.5	8 (29)	12 (43)	8 (29)	28
E13.5	25 (19)	77 (58)	31 (23)	133
E15.5	52 (23)	114 (50)	61 (27)	227
E18.5	76 (27)	152 (53)	61 (21)	289
P0	31 (35)	45 (51)	12 (14)	88
P21	133 (33)	234 (59)	30 (8)	397

Nos. in parenthesis indicate percentage of the total numbers. E, embryonic day; P, day postpartum.

embryonic day 9.5 $Taz^{+/lacZ}$ embryos. At *embryonic day 9.5*, *lacZ* staining was observed in the somitic mesoderm and as in the neuroectoderm within the forebrain and hindbrain (Fig. 1, *E* and *F*). Within the somites, *lacZ* expression was detected in the myotome (Fig. 1*G*). These expression patterns coincide with that of authentic *Taz* expression revealed by in situ hybridization (25).

Early mortality in $Taz^{lacZ/lacZ}$ *mice.* When 309 littermates derived from $Taz^{+/lacZ}$ intercrosses were followed, 24 pups were found dead before 3 wk of age; 9 of 10 dead pups that could be genotyped were homozygous null. Genotyping of the remaining 285 littermates at 3 wk of age identified 90 wild-type (32%), 177 heterozygous (62%), and 18 homozygous (6%) mice, indicating that only one-fifth of the expected Mendelian ratio of $Taz^{lacZ/lacZ}$ mice were alive at weaning (Table 1).

To determine the stage at which homozygous null mice started to die, offspring from $Taz^{+/lacZ}$ intercrosses were genotyped at different embryonic stages. From *embryonic day 8.5* to *15.5*, the distribution of genotypes was close to the 1:2:1 Mendelian ratio (Table 1). At *embryonic day 18.5* and *day 0* postpartum, the numbers of $Taz^{lacZ/lacZ}$ homozygotes were lower than the expected ratio (Table 1), indicating that partial lethality started at the perinatal stage.

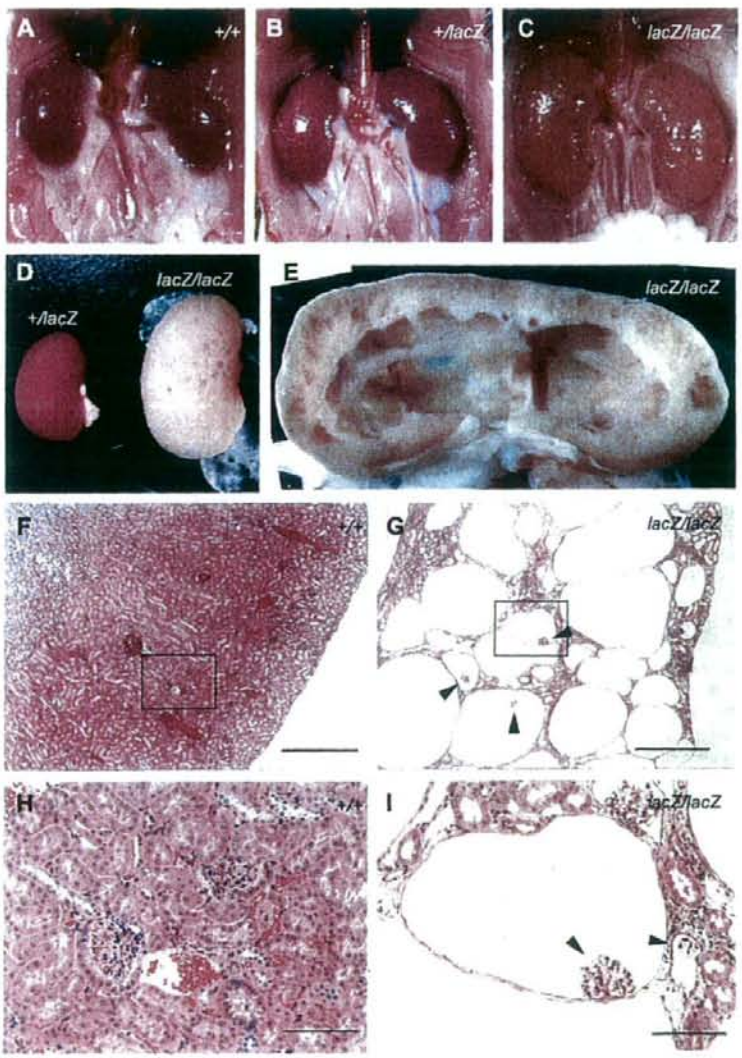

Fig. 2. Enlarged kidneys containing multiple cysts in $Taz^{lacZ/lacZ}$ mice. *A–C*: gross appearance of kidneys of $Taz^{+/+}$ (*A*), $Taz^{-/lacZ}$ (*B*), and $Taz^{lacZ/lacZ}$ (*C*) mice aged 10 wk. $Taz^{lacZ/lacZ}$ kidneys are enlarged, pale, and filled with numerous cysts. *D*: comparison of $TAZ^{+/lacZ}$ and $Taz^{lacZ/lacZ}$ kidneys. *E*: section of a $Taz^{lacZ/lacZ}$ kidney showing dilated calyx and thinned parenchyma containing multiple cysts. *F–I*: histology of $Taz^{+/+}$ (*F* and *H*) and $Taz^{lacZ/lacZ}$ (*G* and *I*) kidneys at low (*F* and *G*) and high (*H* and *I*) magnification. Boxed areas in *F* and *G* are magnified in *H* and *I*, respectively. $Taz^{lacZ/lacZ}$ kidneys exhibit numerous cysts of various sizes that are lined by a flattened epithelial monolayer. Cysts containing a glomerular tuft (arrowheads) are often observed. Scale bars indicate 500 μm (*F* and *G*) or 100 μm (*H* and *I*).

Multiple renal cysts and dilated calyces in $Taz^{lacZ/lacZ}$ mice. To characterize the phenotype that may be related to early mortality, we performed macroscopic and histological examinations on surviving $Taz^{lacZ/lacZ}$ mice. The most prominent abnormalities were first detected in the kidneys. Adult $Taz^{lacZ/lacZ}$ mice showed bilaterally enlarged, pale kidneys (Fig. 2, *C* and *D*). The calyces were extremely dilated, leaving thinned parenchyma containing multiple cysts (Fig. 2*E*). Histological analysis of 10-wk-old $Taz^{lacZ/lacZ}$ mice demonstrated numerous cysts of various sizes replacing most of the renal parenchyma (Fig. 2*G*), whereas no such changes were found in wild-type and $Taz^{+/lacZ}$ kidneys (Fig. 2, *F* and *H*). Cysts were lined by a flattened epithelial monolayer and sometimes contained a glomerular tuft, indicating an origin from Bowman's capsule (Fig. 2, *G* and *I*). The surrounding tissues showed increased interstitial fibrosis in Masson's trichrome staining (data not shown). Notably, these renal changes in $Taz^{lacZ/lacZ}$ mice shared a similar histology to human PKD.

In contrast, calyceal dilatation is uncommon in human PKD. To examine whether the dilation of the pelvis and atrophy of the medulla in $Taz^{lacZ/lacZ}$ kidneys could be secondary to anatomical obstruction in the urinary tract, we injected black ink into the pelvis of *embryonic day 18.5* kidneys. In $Taz^{lacZ/lacZ}$ kidneys, peristaltic passage of urine through the ureter was observed similar to wild-type and heterozygous littermates (data not shown). The urinary bladder was not apparently dilated in $Taz^{lacZ/lacZ}$ embryos at this stage (data not shown). These results suggested that the hydronephrotic changes in $Taz^{lacZ/lacZ}$ kidneys were not due to mechanical obstruction of the urinary tract.

Extrarenal phenotypes in $Taz^{lacZ/lacZ}$ mice. In human ADPKD, extrarenal manifestations are often observed in the liver, pancreas, blood vessels, heart, and other organs. However, examination of adult $Taz^{lacZ/lacZ}$ mice did not reveal obvious abnormalities in these tissues (data not shown). Instead, the lung was unexpectedly affected in $Taz^{lacZ/lacZ}$ mice. Histological examination revealed enlarged air spaces in $Taz^{lacZ/lacZ}$ lungs at the age of 8–9 mo (Fig. 3, *A* and *B*). The mean linear intercept, as a measure of interalveolar wall distance, was significantly greater in $Taz^{lacZ/lacZ}$ mice (149.6 ± 11.5 μm, $n = 4$) than in wild-type mice (51.6 ± 2.1 μm, $n = 4$) (Fig. 3*C*). There were no findings indicative of increased inflammation or fibrosis in $Taz^{lacZ/lacZ}$ lungs. The phenotype of $Taz^{lacZ/lacZ}$ lungs is highly reminiscent of human pulmonary emphysema.

The changes in the kidney and lung were observed in all the homozygous mice derived from two independent recombinant ES clones, although the severity of symptoms varied among individuals. In contrast, no wild-type and $Taz^{+/lacZ}$ mice displayed abnormalities (Figs. 2, *A* and *B*, and 3*A*).

Urinary concentration defects in $Taz^{lacZ/lacZ}$ mice. In addition to multiple cysts and dilated calyces, $Taz^{lacZ/lacZ}$ mice showed signs of polyuria. Indeed, the urinary bladder in $Taz^{lacZ/lacZ}$ mice was typically distended with a large volume of urine (data not shown). Measurement of the 48-h urine frequency and volume revealed that urine volume per void and total volume per day were much higher in $Taz^{lacZ/lacZ}$ mice than in $Taz^{+/lacZ}$ mice (Fig. 4). Measurements of urinary parameters showed polyuria and concentrating defects in $Taz^{lacZ/lacZ}$ mice, as indicated by lower urinary osmolality (Table 2). Overall electrolyte excretion was not enhanced, although excretion of chloride was slightly increased (Table 2), indicating that electrolyte reabsorption remained grossly preserved. Urinary albumin excretion in $Taz^{lacZ/lacZ}$ mice appeared to be increased, although the difference was not statistically significant (Table 2). The polyuria and concentrating defects in $Taz^{lacZ/lacZ}$ mice were not improved by vasopressin administration (data not shown), suggesting that the abnormalities were likely to be nephrogenic rather than due to vasopressin deficiency. Overall, $Taz^{lacZ/lacZ}$ kidneys were characterized by the concomitant occurrence of features that are typical of human PKD, including multicystic formation and urinary concentrating defects, and atypical features such as calyceal dilatation and hydronephrosis.

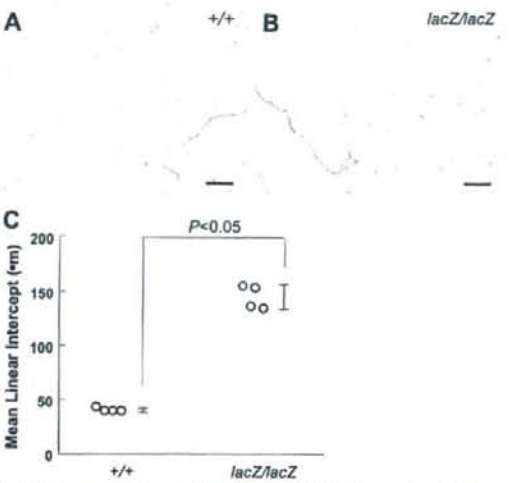

Fig. 3. Pulmonary emphysema-like changes in $Taz^{lacZ/lacZ}$ mice. *A* and *B*: hematoxylin and eosin staining of lung sections of $Taz^{+/+}$ (*A*) and $Taz^{lacZ/lacZ}$ (*B*) mice aged 9 mo. Enlarged air spaces and alveolar wall disruption are observed in the lung of $Taz^{lacZ/lacZ}$ mice. Scale bars indicate 100 μm. *C*: morphometric analysis. Mean linear intercept values are significantly greater in $Taz^{lacZ/lacZ}$ mice ($n = 4$) than wild-type mice ($n = 4$) aged 8–9 mo. A total of 288 lines drawn across the lung section were analyzed for each group. Error bars indicate SDs of the mean.

Cysts primarily originated from glomeruli and proximal tubules in $Taz^{lacZ/lacZ}$ embryos. To determine the time point at which cysts first arose in the kidneys of $Taz^{lacZ/lacZ}$ embryos, we performed histological analysis on kidneys at different embryonic stages. At *embryonic day 13.5*, the branching of ureteric buds and the initial formation of renal vesicles and comma- and S-shaped bodies appeared to be normal in both $Taz^{lacZ/lacZ}$ and wild-type kidneys (Fig. 5, *A* and *B*). At *embryonic day 15.5*, morphological abnormalities were first detected as dilatation of the Bowman's capsules and adjacent tubules in $Taz^{lacZ/lacZ}$ embryos (Fig. 5, *C* and *D*).

At *embryonic day 18.5*, $Taz^{lacZ/lacZ}$ kidneys exhibited tubules with varying degrees of dilatation and multiple cysts in inner cortical and medullary regions (Fig. 5, *E* and *F*). Cyst-lining epithelial cells appeared heterogeneous in morphology; some were flattened and others were rather cuboidal (Fig. 5, *G* and *H*). Glomerular tufts were detected in a small subset of cysts at this stage (Fig. 5, *G* and *H*). The renal pelvis was dilated, and the medulla was atrophic with disturbed formation of the papilla (Fig. 5, *E* and *F*). In contrast, the nephrogenic zone

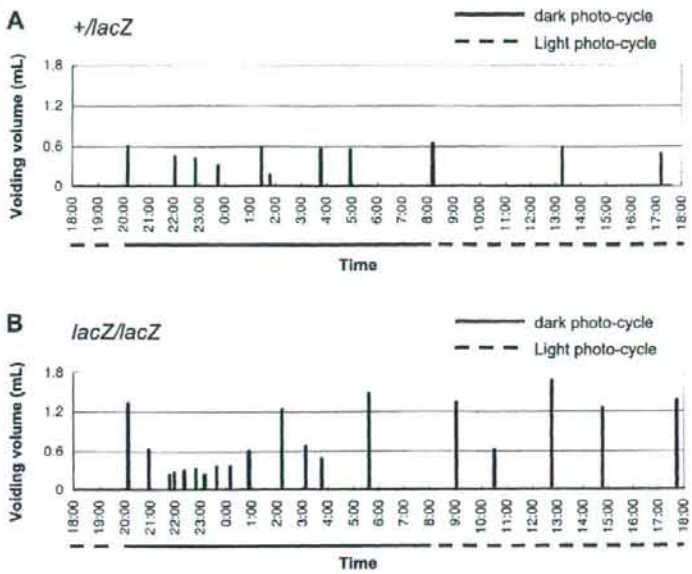

Fig. 4. Representative 24-h urinary frequency/volume records. Mice aged 5–6 mo were subjected to the analysis. Urine volume per void, voiding frequency, and total volume per day are greatly increased in $Taz^{lacZ/lacZ}$ mice (*B*) compared with $Taz^{+/lacZ}$ mice (*A*).

was well-developed in the outer cortex just beneath the capsule and contained many developing nephrons in $TAZ^{lacZ/lacZ}$ and wild-type kidneys (Fig. 5, *E–H*).

We examined the origins of the cysts using segment-specific markers. LTA, a lectin specific for the proximal tubule, stained the majority of epithelial cells lining dilated tubules and cysts in *embryonic day 18.5* $Taz^{lacZ/lacZ}$ embryos (Fig. 6, *A–D*). In contrast, no cysts were stained with DBA, a lectin specific for the collecting duct, at the same stage (Fig. 6, *E–H*). These results suggested that the cystic changes in $Taz^{lacZ/lacZ}$ kidneys primarily originated from glomeruli and proximal tubules during the maturation of induced nephrons.

Expression of Taz in developing kidneys. To correlate the renal phenotype of $Taz^{lacZ/lacZ}$ mice with *Taz* expression, we first performed in situ hybridization on wild-type embryonic kidneys. At *embryonic day 14.5*, *Taz* transcripts were diffusely expressed in both mesenchymal and epithelial cells in the developing metanephros (Fig. 7, *A* and *B*). *Taz* was also present in the ureteric bud (Fig. 7, *A* and *B*). At *embryonic day 16.5*, *Taz* was expressed in mesenchymal and epithelial cells in the nephrogenic zone and collecting ducts (Fig. 7, *C* and *D*).

Table 2. *Defects in urinary concentration in Taz/lacZ/lacZ mice*

	Taz+/+	*Taz/lacZ/lacZ*
n	6	6
Age, wk	20–26	20–26
Body wt, g	36.8±2.1	29.4±3.1*
Water intake, ml/day	6.7±1.4	17.5±2.4*
Urine volume, ml/day	3.56±1.39	10.76±3.02*
Osmolality, mosmol/kgH_2O	2,765±646	855±131*
Urine nitrogen, mg·day^{-1}·g body wt^{-1}	4.11±0.84	3.29±1.36
Creatinine, g·day^{-1}·g body wt^{-1}	32.3±7.0	34.5±13.3
Albumin, g·day^{-1}·g body wt^{-1}	1.91±1.02	29.60±42.49
Na^+, meq·day^{-1}·g body wt^{-1}	0.011±0.004	0.011±0.002
K^+, meq·day^{-1}·g body wt^{-1}	0.034±0.007	0.035±0.009
Cl^-, meq·day^{-1}·g body wt^{-1}	0.017±0.003	0.022±0.006†

Values are means ± SD. *$P < 0.01$ and †$P < 0.05$.

In contrast to in situ hybridization, β-galactosidase activity was observed only in limited cell populations. At *embryonic day 16.5* and *day 0* postpartum, $Taz^{+/lacZ}$ kidneys exhibited sporadic *lacZ* expression in glomeruli and capillary endothelial cells that were positive for CD31 (Fig. 7, *E*, *F*, and *J–L*), indicating that *lacZ* expression may only reflect a part of the authentic *Taz* expression, possibly due to disruption of critical genomic sequences. In $Taz^{lacZ/lacZ}$ homozygous kidneys, β-galactosidase activity was detected in stromal(-like) cells, especially in the outer cortical region as well as in glomeruli and capillary endothelial cells (Fig. 7, *G–I*, *M*, and *N*). In addition, some cysts are lined by *lacZ*-positive cells in *day 0* postpartum $Taz^{lacZ/lacZ}$ kidneys (Fig. 7*O*).

Expression of cystic disease transcripts and proteins in $Taz^{lacZ/lacZ}$ *kidneys.* To find clues to the mechanism underlying the renal phenotype of $Taz^{lacZ/lacZ}$ mice, we analyzed the expression of genes involved in human PKD. No alterations in the levels of *Pkd1* and *Pkd2* mRNA and their products, polycystin-1 and polycystin-2, were observed at *embryonic day 15.5* and *18.5* by real-time RT-PCR (Fig. 8, *A* and *B*) and Western blotting (Fig. 8*D*). Also, the expression of *Pkhd1*, a gene linked to ARPKD, was not different between wild-type and $Taz^{lacZ/lacZ}$ kidneys (Fig. 8*C*). These results indicated that renal cyst formation induced by *Taz*-null mutation was not due to changes in the expression of *Pkd1*, *Pkd2*, and *Pkhd1* at the perinatal stage.

Expression of genes involved in water metabolism in $Taz^{lacZ/lacZ}$ *kidneys.* The absence of changes in the expression of cystic disease genes and concomitant diabetes insipidus-like state led us to speculate that unique pathogenetic mechanisms might

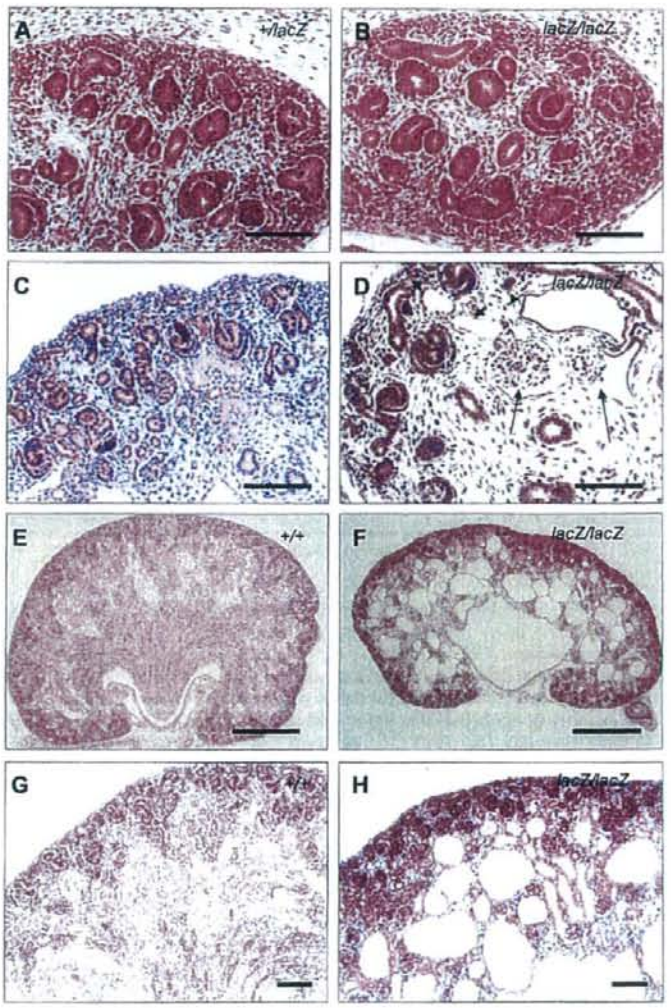

Fig. 5. Histological examination of developing kidneys in control (*A*, *C*, *E*, and *G*) and $Taz^{lacZ/lacZ}$ (*B*, *D*, *F*, and *H*) embryos. *A* and *B*: at *embryonic day 13.5*, branching of ureteric buds and formation of renal vesicles and comma- and S-shaped bodies are observed in $Taz^{lacZ/lacZ}$ (*B*) as well as wild-type and $Taz^{+/lacZ}$ (*A*) kidneys. *C* and *D*: at *embryonic day 15.5*, dilatation of Bowman's capsules (arrows) and adjacent tubules (arrowheads) are detected in $Taz^{lacZ/lacZ}$ kidneys (*D*) but not in wild-type kidneys (*C*). *E–H*: at *embryonic day 18.5*, the atrophic medulla contains multiple cysts of various sizes in $Taz^{lacZ/lacZ}$ kidneys (*F* and *H*). The pelvis is dilated and the papilla is not well formed (*F*). These changes are not observed in wild-type kidneys (*E* and *G*). The nephrogenic zone is present in the outer cortex just beneath the capsule in $Taz^{lacZ/lacZ}$ (*H*) and wild-type (*G*) kidneys. Scale bars indicate 100 μm (*A–D*, *G*, and *H*) and 500 μm (*E* and *F*).

underlie the renal phenotypes in $Taz^{lacZ/lacZ}$ kidneys. To explore the basis for disturbed water metabolism, we investigated the expression of genes and proteins that are involved in renal water transport. Although the urinary concentration defects in $Taz^{lacZ/lacZ}$ mice were resistant to exogenous vasopressin, real-time RT-PCR analysis showed that the expression of the arginine vasopressin receptor 2 gene (*Avpr2*) was largely unaffected in $Taz^{lacZ/lacZ}$ kidneys (Fig. 9*A*). The expression of aquaporin (*Aqp-1*, *-2*, and *-3*) water channels that are involved in renal water reabsorption (28) was not different among wild-type, heterozygous, and homozygous mutant kidneys (Fig. 9*B*). Immunostaining demonstrated that aquaporin-3 was localized in the basolateral membrane of epithelial cells in both $Taz^{lacZ/lacZ}$ and control $Taz^{+/lacZ}$ kidneys (Fig. 9, *C* and *D*), indicating that the polarity of aquaporin-3 localization in $Taz^{lacZ/lacZ}$ epithelial cells was intact. In $Taz^{lacZ/lacZ}$ kidneys, aquaporin-3 was expressed in many noncystic tubules and a few cysts (Fig. 9*D*), indicating an origin from the renal collecting ducts. Aquaporin-2 was also expressed similarly in collecting ducts in heterozygous and homozygous kidneys at *embryonic day 18.5* (Fig. 9, *E* and *F*). These results indicated that the renal phenotype of $Taz^{lacZ/lacZ}$ mice was not caused by changes in the expression of *Avpr2* or aquaporins.

DISCUSSION

In the present study, we demonstrate that a null mutation of *Taz* results in the formation of bilateral multicystic kidneys and

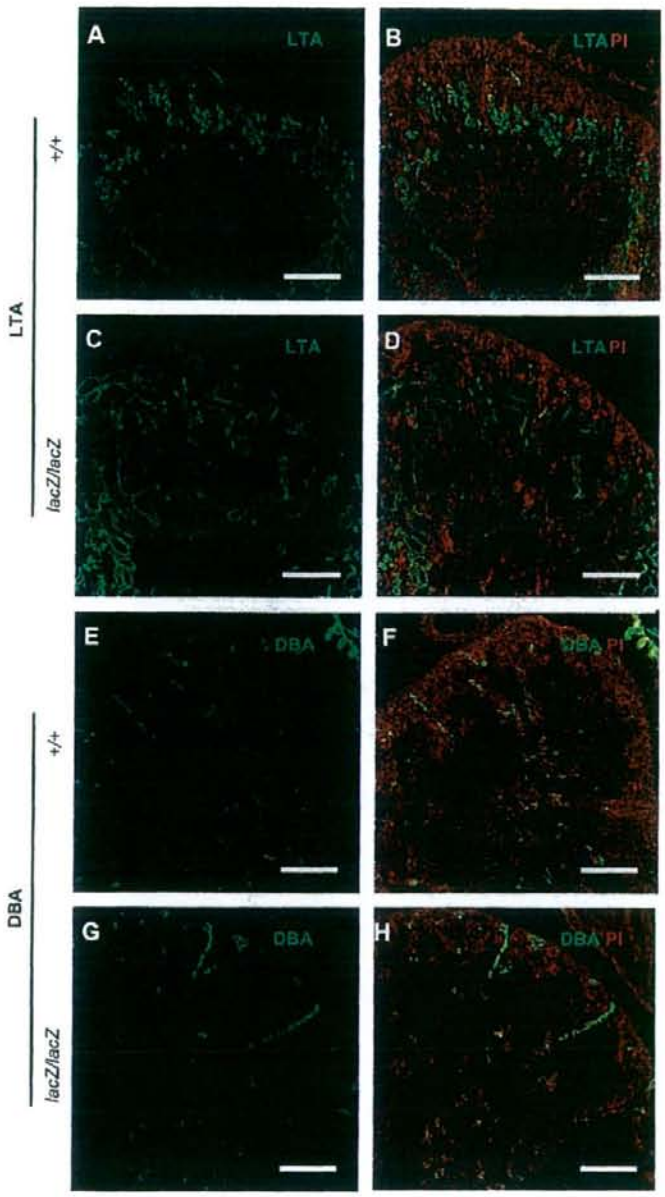

Fig. 6. Proximal tubular dilatation leading to cyst formation in $Taz^{lacZ/lacZ}$ embryos. Sections were stained with *Lotus tetragonolobus* agglutinin (LTA; *A–D*) or *Dolichos biflorus* agglutinin (DBA; *E–H*) in wild-type (*A*, *B*, *E*, and *F*) and $Taz^{lacZ/lacZ}$ (*C*, *D*, *G*, and *H*) kidneys at *embryonic day 18.5*. *B*, *D*, *F*, and *H* show costaining with propidium iodide and lectins. Epithelial cells lining dilated tubules and cysts stain positive with LTA but not with DBA in $Taz^{lacZ/lacZ}$ kidneys. Scale bars indicate 250 μm.

diffuse emphysematous changes in the lung. Renal cysts mainly originate from the glomeruli and proximal tubules around *embryonic day 15.5*, as revealed by histological features and lectin marker staining. Later, the renal changes are accompanied by pelvic dilatation and atrophy of the medulla, indicating hydronephrosis. After birth, only one-fifth of TAZ-deficient homozygotes grow to adulthood. The early mortality may be due to water and electrolyte imbalance and/or respiratory insufficiency. Surviving mutants demonstrate progressive renal changes with massive polyuria. The renal phenotype of

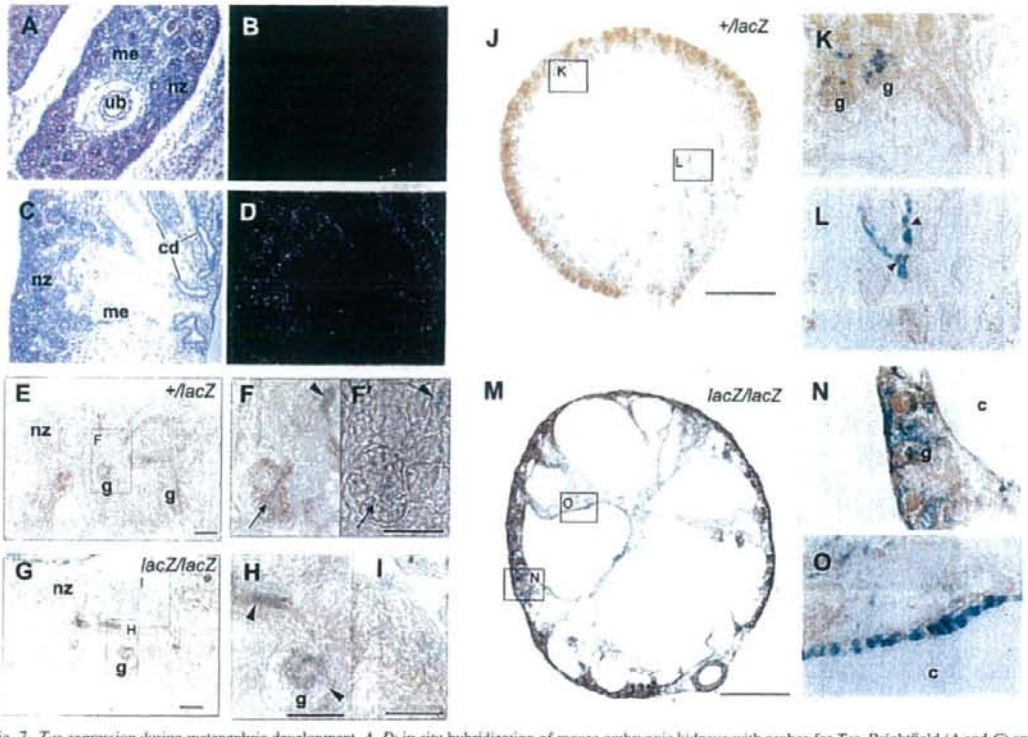

Fig. 7. *Taz* expression during metanephric development. *A–D*: in situ hybridization of mouse embryonic kidneys with probes for *Taz*. Brightfield (*A* and *C*) and darkfield (*B* and *D*) images of *embryonic day 14.5* (*A* and *B*) and *embryonic day 16.5* (*C–F*) kidneys are shown. *A* and *B*: at *embryonic day 14.5*, *Taz* transcripts are diffusely detected in metanephric mesenchymal and epithelial cells and the ureteric bud. *C* and *D*: at *embryonic day 16.5*, *Taz* is expressed in mesenchymal and epithelial cells in the nephrogenic zone. *Taz* is also expressed in the collecting ducts. *E–O*: β-galactosidase activity in $Taz^{+/lacZ}$ (*E, F*, and *J–L*) and $Taz^{lacZ/lacZ}$ (*G–I* and *M–O*) kidneys at *embryonic day 16.5* (*E–I*) and *day 0* postpartum (P0; *J–O*). *E, F*, and *F'*, in *embryonic day 16.5* $Taz^{+/lacZ}$ kidneys, X-gal staining (blue) is observed in glomeruli (arrows) and CD31-stained (brown) capillary endothelial cells (arrowheads). X-gal staining with (*F*) and without (*F'*) CD31 staining is shown. *G–I*: in *embryonic day 16.5* $Taz^{lacZ/lacZ}$ kidneys, X-gal staining is observed in stromal(-like) cells (open arrowheads in *I*) as well as in glomeruli and capillary endothelial cells (filled arrowheads in *H*). *J–L*: in P0 $Taz^{+/lacZ}$ kidneys, scattered X-gal staining is observed in glomeruli (*K*) and capillary endothelial cells (*L*). *M–O*: in P0 $Taz^{lacZ/lacZ}$ kidneys, X-gal staining is observed in outer cortical stromal cells, glomeruli, and capillaries (*N*). Some cysts are lined by X-gal-positive cells (*O*). Sections of P0 kidney were counterstained with Orange G. c, cyst; cd, collecting duct; g, glomerulus; me, mesenchyme; nz, nephrogenic zone; ub, ureteric bud. Scale bars indicate 50 μm (*E* and *I*) and 500 μm (*J* and *M*).

TAZ-deficient mice is reminiscent of human renal cystic diseases, as represented by PKD, but is distinct in that it manifests as severe hydronephrosis and urinary concentration defects.

Comparison of the renal phenotype of TAZ-deficient mice to human cystic kidney diseases. In human ADPKD, the epithelial-lined cysts originate from any segment of the nephron and collecting ducts, and in ARPKD the cysts mainly originate from the collecting ducts (3, 10). In contrast, the cysts in TAZ-deficient kidneys mainly originate from the glomeruli and proximal tubules. However, patients with early onset ADPKD may develop glomerular cysts, suggesting that cyst formation in the proximal nephrons may be an early manifestation of ADPKD (11, 15). Consistently, *Pkd1*-null mice start to exhibit cyst formation at *embryonic day 15.5* in the proximal tubule (20). Other animal models of PKD, such as the *cpk/cpk* mice and the Han:SPRD *cy/+* rats, have also shown cysts originating predominantly from the proximal tubule (39). Studies of human fetuses with ARPKD have shown cysts originating from proximal tubules. Thus the renal phonotype of TAZ-deficient mice may recapitulate the early phase of human PKD.

However, no apparent differences in the expression of PKD genes, *Pkd1*, *Pkd2*, and *Pkhd1*, are detected in the kidneys of wild-type and TAZ-deficient embryos before birth. This finding indicates that cyst formation in TAZ-deficient kidneys is not due to changes in the expression of these cystic disease genes. Polycystin-1 and -2, proteins encoded by ADPKD genes *PKD1* and *PKD2*, respectively, are membrane glycoproteins that can associate with each other to form a complex in the primary cilium of renal epithelial cells (2, 10, 19). The polycystin complex is implicated in cell cycle regulation, intracellular calcium regulation, and maintenance of cellular polarity (2, 10, 19). Polyductin/fibrocystin, the protein encoded by *PKHD1*, is also a large transmembrane protein. Considering the possible interaction of TAZ with membrane-associated PDZ domain-containing proteins, it may still be possible that TAZ and the cystic disease proteins share a common pathway

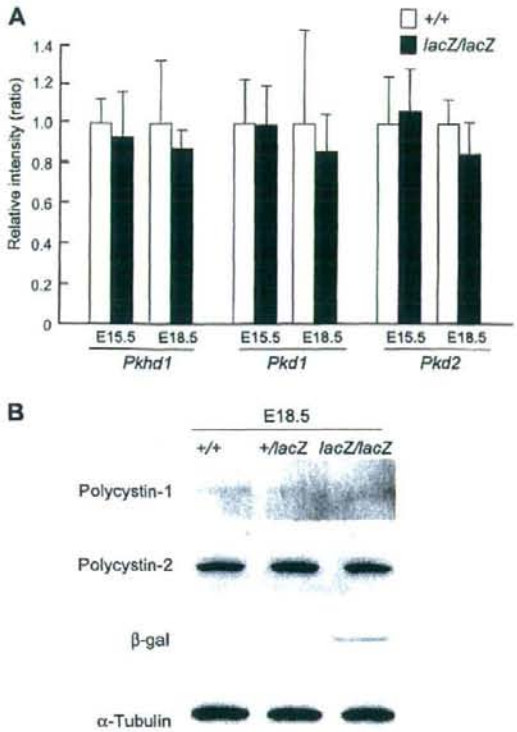

Fig. 8. Real-time RT-PCR analysis and Western blotting of cystic disease genes and proteins. *A*: real-time RT-PCR. Total RNA samples were prepared from *embryonic day 15.5* and *18.5* wild-type (*+/+*) and homozygous (*lacZ/lacZ*) kidneys. The abundance of transcripts for *Pkd1*, *Pkd2*, and *Pkhd1* was measured relative to the internal control *Gapdh*. Error bars indicate SDs of the mean (n = 5). For all threes genes at both stages, the expression in homozygous mutant kidneys is not statistically different from wild-type kidney ($P > 0.05$). *B*: Western blotting for polycystin-1 and polycystin-2. Protein levels of polycystin-1 and -2 are not different among wild-type, $Taz^{+/lacZ}$, and $Taz^{lacZ/lacZ}$ kidneys at *embryonic day 18.5*. Blotting for β-galactosidase shows intensities corresponding to the copy number of the *lacZ* gene. Blotting for α-tubulin serves as an internal control.

involved in normal epithelial function and structural integrity. However, taken together with the pathological differences from human PKD, distinct mechanisms may be involved in the renal phenotype of TAZ-deficient mice.

Recently, Hossain et al. (16) also reported the development of cystic kidney disease in TAZ/Wwtr1-deficient mice. Their study suggested that the loss of renal cilia integrity and down-regulation of several genes, including *Pkhd1*, might be associated with the development of renal cysts in TAZ-deficient mice. Independently, Tian et al. (35) have reported that polycystin-2 is overexpressed in adult TAZ-deficient kidneys as a result of decreased ubiquitin-mediated degradation. In the present study, no changes in fibrocystin or polycystin-2 expression are observed in TAZ-deficient kidneys during the prenatal stage, when cyst formation starts. Abnormalities in fibrocystin and polycystin-2 may be involved in later stages of disease progression rather than initial cystogenesis.

Comparison of the renal phenotype of TAZ-deficient mice with human nephrogenic diabetes insipidus. A major difference between the renal phenotype of TAZ-deficient mice and human PKD is the presence of severely dilated calyces and massive polyuria. Although humans with ADPKD and ARPKD may have urinary concentration defects (6, 21), severe polyuria and hydronephrosis are not typical clinical features. TAZ-deficient mice have normal daily excretion of sodium and potassium, indicating that tubular electrolyte reabsorption is well preserved. The relatively low urine osmolality compared with wild-type together with impaired response to exogenous vasopressin are characteristic of nephrogenic diabetes insipidus. Hydronephrosis may be secondary to polyuria, as seen in congenital progressive hydronephrosis (*cph*) mutant mice (22). Thus the renal phenotype of TAZ-deficient mice is characterized by two distinct pathophysiological processes, cyst formation and urinary concentration defects.

Nephrogenic diabetes insipidus is caused by the inability of the renal collecting ducts to reabsorb water in response to vasopressin. About 90% of affected patients have mutations in the *AVPR2* gene, whereas the remaining 10% of patients are caused by *AQP2* gene mutations (28). However, TAZ-knockout kidneys do not show major abnormalities in the levels of expression of *Avpr2*, *Aqp2*, and *Aqp3*. In addition, the apical-basolateral polarity of aquaporin-2 and aquaporin-3 is preserved in both cystic and noncystic collecting ducts at embryonic and postnatal stages. These findings suggest that the polyuria and hydronephrosis in TAZ-deficient mice do not arise from major defects in the expression or localization of the V_2 vasopressin receptor, aquaporin-2, or aquaporin-3. Elucidation of the mechanism underlying the concentration defects in TAZ-deficient kidney may reveal novel pathways regulating renal water transport.

Possible requirement of TAZ for normal kidney development. The kidney develops through reciprocal interactions between the metanephric mesenchyme and the ureteric bud epithelium during embryogenesis (8, 36, 40). The ureteric bud grows into the metanephric mesenchyme and branches to form the collecting duct system while the mesenchyme adjacent to the tips of the ureteric bud is induced to condense and undergo a mesenchymal-to-epithelial transition. The resultant renal vesicle further differentiates into comma- and then S-shaped bodies. Morphogenesis and patterning of the epithelial structures lead to the formation and functional maturation of nephron segments including the glomerulus, the proximal tubule, the loop of Henle, and the distal tubule. Recent advances in gene targeting experiments have greatly contributed to the understanding of molecular mechanisms underlying the early "inductive" phase of kidney development. However, it remains largely unknown how each nephron segment is specified and functionally matures during the late phase of kidney development.

In situ hybridization and β-galactosidase staining demonstrated that *Taz* is diffusely expressed throughout the kidney. *Taz* expression is most intense in the nephrogenic zone during kidney development and is found in both mesenchymal and epithelial cells. *Taz* is not restricted to a specific segment of the nephron. Capillary endothelial cells also express *Taz*. *LacZ* expression is relatively scant and scattered compared with the pattern of in situ hybridization. This difference may be caused

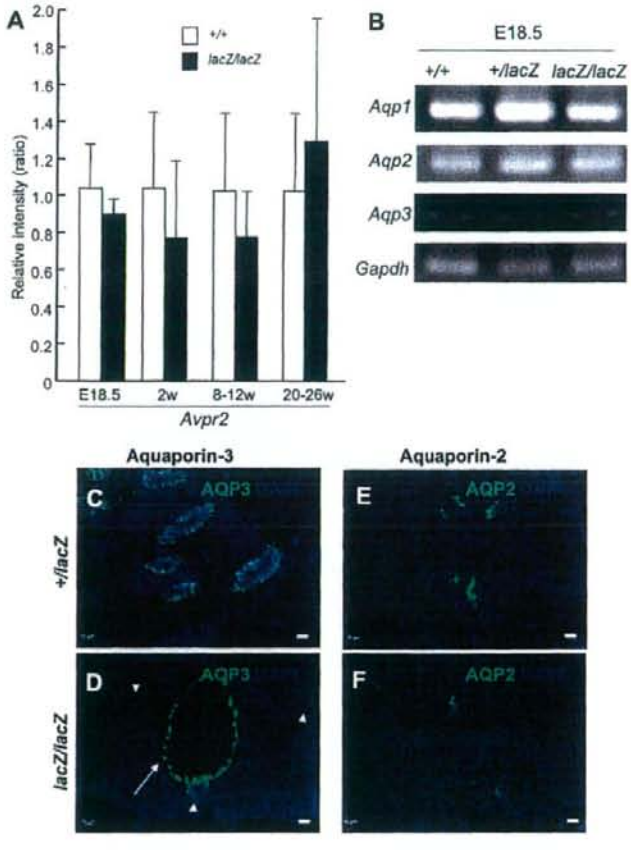

Fig. 9. Expression of genes involved in water transport. *A*: real-time RT-PCR. Total RNA samples were prepared from *embryonic day 18.5* and 2-wk-old wild-type (+/+) and homozygous (*lacZ/lacZ*) kidneys. The abundance of transcripts for *Avpr2* was measured relative to the internal control *Gapdh*. Error bars indicate SDs of the mean; $n = 5$ (+/+) and 5 (*lacZ/lacZ*) at *embryonic day 18.5*; $n = 4$ (+/+) and 3 (*lacZ/lacZ*) at 2 wk; $n = 8$ (+/+) and 6 (*lacZ/lacZ*) at 8–12 wk; $n = 4$ (+/+) and 4 (*lacZ/lacZ*) at 20–26 wk. No statistically significant difference is detected in the expression of *Avpr2* between +/+ and *lacZ/lacZ* kidneys ($P > 0.05$). *B*: RT-PCR analysis of *Aquaporin-1*, *-2*, and *-3* expression. Total RNA samples were prepared from *embryonic day 18.5* wild-type (+/+), heterozygous (+/*lacZ*), and homozygous (*lacZ/lacZ*) kidneys. The levels of *Aquaporin-1*, *-2*, and *-3* transcripts are not different among wild-type, heterozygous, and homozygous kidneys. RT-PCR for *Gapdh* served as an internal control. *C–F*: immunofluorescence staining of aquaporins. Sections were stained for aquaporin-3 (*C* and *D*) or aquaporin-2 (*E* and *F*) in $Taz^{+/lacZ}$ (*C* and *E*) and $Taz^{lacZ/lacZ}$ (*D* and *F*) kidneys at *embryonic day 18.5*. All sections were costained with 4′,6-diamidine-2-phenylindole. Aquaporin-3 is localized in the basolateral membrane of epithelial cells in some cysts (arrow) as well as in noncystic tubules (arrowheads) in $Taz^{lacZ/lacZ}$ kidneys. Aquaporin-2 is also expressed similarly in collecting ducts in heterozygous and homozygous kidneys. Scale bars indicate 10 μm.

by deletion or disruption of critical enhancer element(s) during the generation of the targeted mutation.

In TAZ-deficient kidneys, most, but not all, of the cyst epithelium is *lacZ*-negative. In contrast, stromal cells, especially in the nephrogenic zone, show strong *lacZ* expression in TAZ-deficient kidneys. This finding indicates that TAZ may be crucial for gene expression in stromal cells supporting normal nephric development.

Pulmonary emphysematous changes in TAZ-deficient mice. In addition to renal cyst formation, TAZ-deficient mice demonstrate severely enlarged air spaces in the lung. This finding is morphologically reminiscent of human pulmonary emphysema, whose genetic pathogenesis is poorly understood. Only a congenital form of emphysema is known to be caused by a deficiency of α-antitrypsin, but its expression was not affected in TAZ-deficient mice (our unpublished data).

Pulmonary emphysema, as a manifestation of COPD, is regarded as a multifactorial disorder triggered by environmental factors such as cigarette smoking and pollutants. Although genetic factors involved in protease/antiprotease balance have been considered as possible determinants of susceptibility to emphysematous changes, the molecular pathogenesis is still unknown. In mice, emphysema-like pulmonary changes can be caused by deficiency in surfactant proteins SP-C or SP-D, possibly through increased activity of matrix metalloproteases (9, 38). Interestingly, TAZ has been reported to be a coactivator for the transcription factor TTF-1/Nkx2.1 and upregulates the expression of SP-C in respiratory epithelial cells (5). However, SP-C expression was not apparently affected in TAZ-deficient lungs (unpublished observations), so different mechanisms may generate the emphysematous changes in TAZ-deficient lungs.

The coexistence of renal and pulmonary abnormalities observed in TAZ-deficient mice has not been described before. However, there are similarities in the embryonic development of the kidney and lung. Both involve common processes, e.g., branching morphogenesis and common signaling pathways such as sonic hedgehog, fibroblast growth factor, and bone morphogenetic protein (17, 41). These similarities raise the possibility that TAZ may be an effector in a common pathway that is involved in both lung and kidney development. Although the apical-basolateral polarity of epithelial cells in collecting ducts is not impaired in TAZ-deficient kidneys, further examination of the processes of epithelial tubule formation in TAZ-deficient kidneys and lungs may reveal a